Article

IL-33-activated ILC2s induce tertiary lymphoid structures in pancreatic cancer

https://doi.org/10.1038/s41586-024-08426-5

Received: 25 October 2021

Accepted: 19 November 2024

Published online: 15 January 2025

Open access

Check for updates

Masataka Amisaki[1,2,19], Abderezak Zebboudj[1,2,19], Hiroshi Yano[3,4,5,6,7], Siqi Linsey Zhang[1,2], George Payne[1,2], Adrienne Kaya Chandra[1,2], Rebecca Yu[1,2], Pablo Guasp[1,2], Zachary M. Sethna[1,2,8], Akihiro Ohmoto[1,2], Luis A. Rojas[1,2], Charlotte Cheng[1,2], Theresa Waters[1,2], Alexander Solovyov[8], Stephen Martis[8], Ashley S. Doane[8], Charlotte Reiche[1,2], Emmanuel M. Bruno[1,2], Martina Milighetti[1,2,8], Kevin Soares[2,9], Zagaa Odgerel[1,2], John Alec Moral[2], Julia N. Zhao[2], Mithat Gönen[10], Rui Gardner[11], Alexei V. Tumanov[12], Abdul G. Khan[13], Olivia Vergnolle[13], Elisabeth K. Nyakatura[13], Ivo C. Lorenz[13], Manuel Baca[13], Erin Patterson[14], Benjamin Greenbaum[8,10,14,15], David Artis[3,4,5,6,7], Taha Merghoub[16,17,18] & Vinod P. Balachandran[1,2,9,14] ✉

Tertiary lymphoid structures (TLSs) are de novo ectopic lymphoid aggregates that regulate immunity in chronically inflamed tissues, including tumours. Although TLSs form due to inflammation-triggered activation of the lymphotoxin (LT)–LTβ receptor (LTβR) pathway[1], the inflammatory signals and cells that induce TLSs remain incompletely identified. Here we show that interleukin-33 (IL-33), the alarmin released by inflamed tissues[2], induces TLSs. In mice, *Il33* deficiency severely attenuates inflammation- and LTβR-activation-induced TLSs in models of colitis and pancreatic ductal adenocarcinoma (PDAC). In PDAC, the alarmin domain of IL-33 activates group 2 innate lymphoid cells (ILC2s) expressing LT that engage putative LTβR$^+$ myeloid organizer cells to initiate tertiary lymphoneogenesis. Notably, lymphoneogenic ILC2s migrate to PDACs from the gut, can be mobilized to PDACs in different tissues and are modulated by gut microbiota. Furthermore, we detect putative lymphoneogenic ILC2s and IL-33-expressing cells within TLSs in human PDAC that correlate with improved prognosis. To harness this lymphoneogenic pathway for immunotherapy, we engineer a recombinant human IL-33 protein that expands intratumoural lymphoneogenic ILC2s and TLSs and demonstrates enhanced anti-tumour activity in PDAC mice. In summary, we identify the molecules and cells of a druggable pathway that induces inflammation-triggered TLSs. More broadly, we reveal a lymphoneogenic function for alarmins and ILC2s.

Secondary lymphoid organs (SLOs) are key mammalian structures that coordinate immune responses to acute tissue injury. SLOs drain regional tissue antigens and colocalize immune cells that sample antigens with effector immune cells to thereby coordinate a structural and cellular strategy to patrol tissues and rapidly mount adaptive immune responses. However, in chronic inflammatory states, hosts must develop lymphoid organs ectopically within inflamed tissues to boost the intensity and proximity of the immune response. Such ectopic lymphoid organs, termed TLSs, are ubiquitous structures that regulate immunity in chronically inflamed tissues[3], including infection, inflammation and cancer.

In cancer, hosts ostensibly develop TLSs[3] in any tissue that can boost endogenous[3] and therapeutic[4–6] anti-tumour immunity. Therefore, new strategies to induce TLSs are attractive, as most human tumours have fewer infiltrating immune cells (immunologically cold), rendering them resistant to current immunotherapies. However, in contrast to SLOs

[1]Immuno-Oncology Service, Human Oncology and Pathogenesis Program, Memorial Sloan Kettering Cancer Center, New York, NY, USA. [2]Hepatopancreatobiliary Service, Department of Surgery, Memorial Sloan Kettering Cancer Center, New York, NY, USA. [3]Jill Roberts Institute for Research in Inflammatory Bowel Disease, Weill Cornell Medicine, New York, NY, USA. [4]Friedman Center for Nutrition and Inflammation, Weill Cornell Medicine, Cornell University, New York, NY, USA. [5]Allen Discovery Center for Neuroimmune Interactions, New York, NY, USA. [6]Joan and Sanford I. Weill Department of Medicine, Division of Gastroenterology and Hepatology, Weill Cornell Medicine, Cornell University, New York, NY, USA. [7]Department of Microbiology and Immunology, Weill Cornell Medicine, Cornell University, New York, NY, USA. [8]Computational Oncology Service, Department of Epidemiology & Biostatistics, Memorial Sloan Kettering Cancer Center, New York, NY, USA. [9]David M. Rubenstein Center for Pancreatic Cancer Research, Memorial Sloan Kettering Cancer Center, New York, NY, USA. [10]Department of Biostatistics & Epidemiology, Memorial Sloan Kettering Cancer Center, New York, NY, USA. [11]Flow Cytometry Core Facility, Memorial Sloan Kettering Cancer Center, New York, NY, USA. [12]Department of Microbiology, Immunology & Molecular Genetics, University of Texas Health Science Center at San Antonio, San Antonio, TX, USA. [13]Tri-Institutional Therapeutics Discovery Institute, New York, NY, USA. [14]The Olayan Center for Cancer Vaccines, Memorial Sloan Kettering Cancer Center, New York, NY, USA. [15]Physiology, Biophysics & Systems Biology, Weill Cornell Medicine, Weill Cornell Medical College, New York, NY, USA. [16]Sandra and Edward Meyer Cancer Center, Weill Cornell Medicine, Weill Cornell Medical College, New York, NY, USA. [17]Parker Institute for Cancer Immunotherapy, Weill Cornell Medicine, New York, NY, USA. [18]Swim Across America and Ludwig Collaborative Laboratory, Department of Pharmacology, Weill Cornell Medicine, New York, NY, USA. [19]These authors contributed equally: Masataka Amisaki, Abderezak Zebboudj. ✉e-mail: balachav@mskcc.org

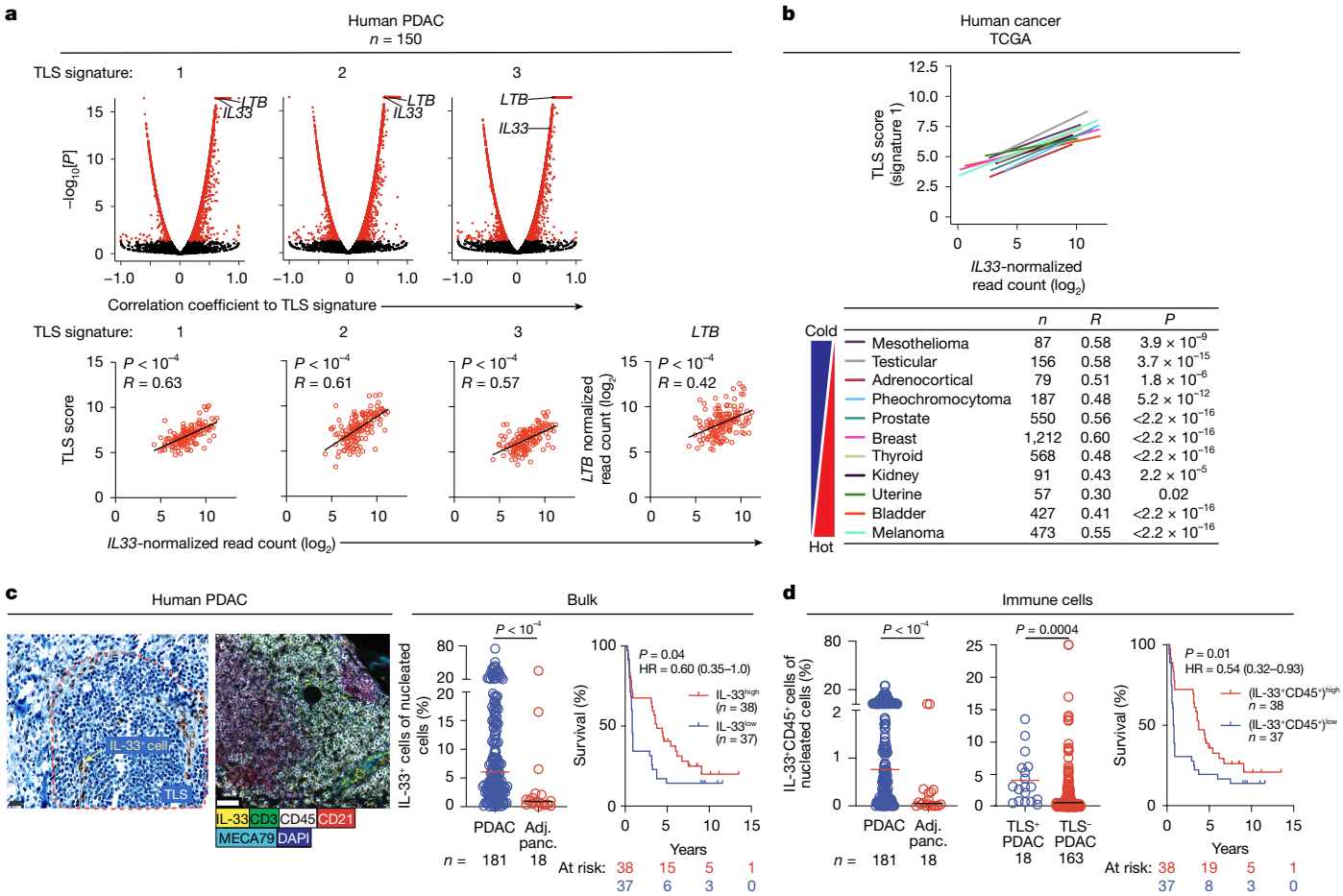

Fig. 1 | *IL33* expression correlates with TLS transcriptional signatures in human tumours. a,**b**, Unbiased correlation of bulk tumour mRNA gene expression to TLS transcriptional signatures (TLS signatures 1 (ref. 4), 2 (ref. 7) and 3 (ref. 8)) in human PDAC (**a**, top). Correlation of bulk tumour *IL33* mRNA expression to TLS transcriptional signatures and *LTB* in human PDAC (**a**, bottom) and human tumours (TLS signature 1; **b**). **c**,**d**, Immunohistochemistry (**c**, left) and immunofluorescence (**c**, right), and the immunofluorescence-quantified frequency of bulk IL-33$^+$ cells (**c**) and IL-33$^+$CD45$^+$ cells (**d**), and association with survival (**c** and **d**) in human PDAC. The dotted red line in **c** shows the putative TLS. Adj. panc., adjacent pancreatic tissue; HR, hazard ratio. *n* represents the number of tumours (**a**–**c**) or patients (survival; **c** and **d**). High and low (in the survival plots in **c** and **d**) represent ≥ (high) or < (low) the median frequency of the cohort. Horizontal bars in dot plots indicate the median (**c**, **d**). *P* values were calculated using two-sided Pearson correlation (**a** and **b**), two-tailed Mann–Whitney *U*-test (**c** (left) and **d** (left and middle)) and two-sided log-rank test (**c** (right) and **d** (right)). For **c**, scale bars, 20 µm (left) and 50 µm (right).

that are preformed, TLSs assemble de novo in chronically inflamed tissues. As such, inflammation-induced drivers and cells that induce TLSs remain incompletely identified.

IL-33 mediates lymphoneogenesis

To identify candidate inflammatory signals that induce TLSs in tumours, we searched for genes with expression that positively correlated with known TLS transcriptional signatures[4,7,8] in PDAC—a lethal model cold tumour with few TLSs but, when present, higher intratumoural TLS density boosts immunity and is correlated with longer survival[9]. As TLSs are identified by inducing chemokines and resident cells (activated T cells, B cells, dendritic cells (DCs) and myeloid cells)[3], we selected three principally non-overlapping transcriptional signatures that identify intratumoural TLSs based on chemokines[7], cells[8] or other immunotherapy-promoting factors[4]. We found that expression of *IL33*—which encodes the alarmin canonically released in inflamed tissues[10]—correlated with all three TLS signatures (Fig. 1a) and with *LTB* expression (*LTB* encodes the TLS-inducing cytokine[11] LTβ) in three different PDAC cohorts ($n = 328$ PDACs; Fig. 1a, Extended Data Fig. 1a and Supplementary Table 1), as well as in other cold and hot tumours ($n = 11$ histologies, 3,887 tumours; Fig. 1b and Extended Data Fig. 1b). Within TLSs in PDAC, we detected IL-33$^+$ cells, including IL-33$^+$ immune cells (Fig. 1c (left), Extended Data Fig. 1c,d and Supplementary Table 2) that were more abundant in tumours compared with in adjacent pancreatic tissues (Fig. 1c (middle) and 1d (left)), and enriched in tumours with TLSs compared with those without (Fig. 1d (middle)). Furthermore, higher intratumoural IL-33$^+$ bulk and IL-33$^+$ immune cell densities were correlated with improved PDAC survival (Fig. 1c (right) and 1d (right)). Together, these results identified a correlation between IL-33 and TLSs in cancer.

To probe a potential causative link between IL-33 and TLSs, we used a *Kras*- and *Trp53*-driven orthotopically implanted PDAC mouse model (PDAC mice) with few baseline TLSs to first examine whether endogenous *Il33* is required for de novo lymphoneogenesis. We found that activating the LTβ receptor (LTβR)[12]—a canonical signal for TLS neogenesis[1,3,11,13]—generated intratumoural TLSs and controlled tumours in wild-type (WT) but not in *Il33*$^{-/-}$ PDAC mice (Fig. 2a (left) and Extended Data Fig. 2a). *Il33* was also required for inflammation-induced lymphoneogenesis, as oral dextran sulfate sodium (DSS), which provokes chemical colitis (DSS-colitis mice)[14] and models human inflammatory bowel disease, stimulated colonic lymphoid aggregates in WT but not in *Il33*$^{-/-}$ mice (Fig. 2a (right)), exacerbating weight loss and diminishing survival (Extended Data Fig. 2b). Endogenous *IL33* is therefore required to induce TLSs in models of cancer and inflammation.

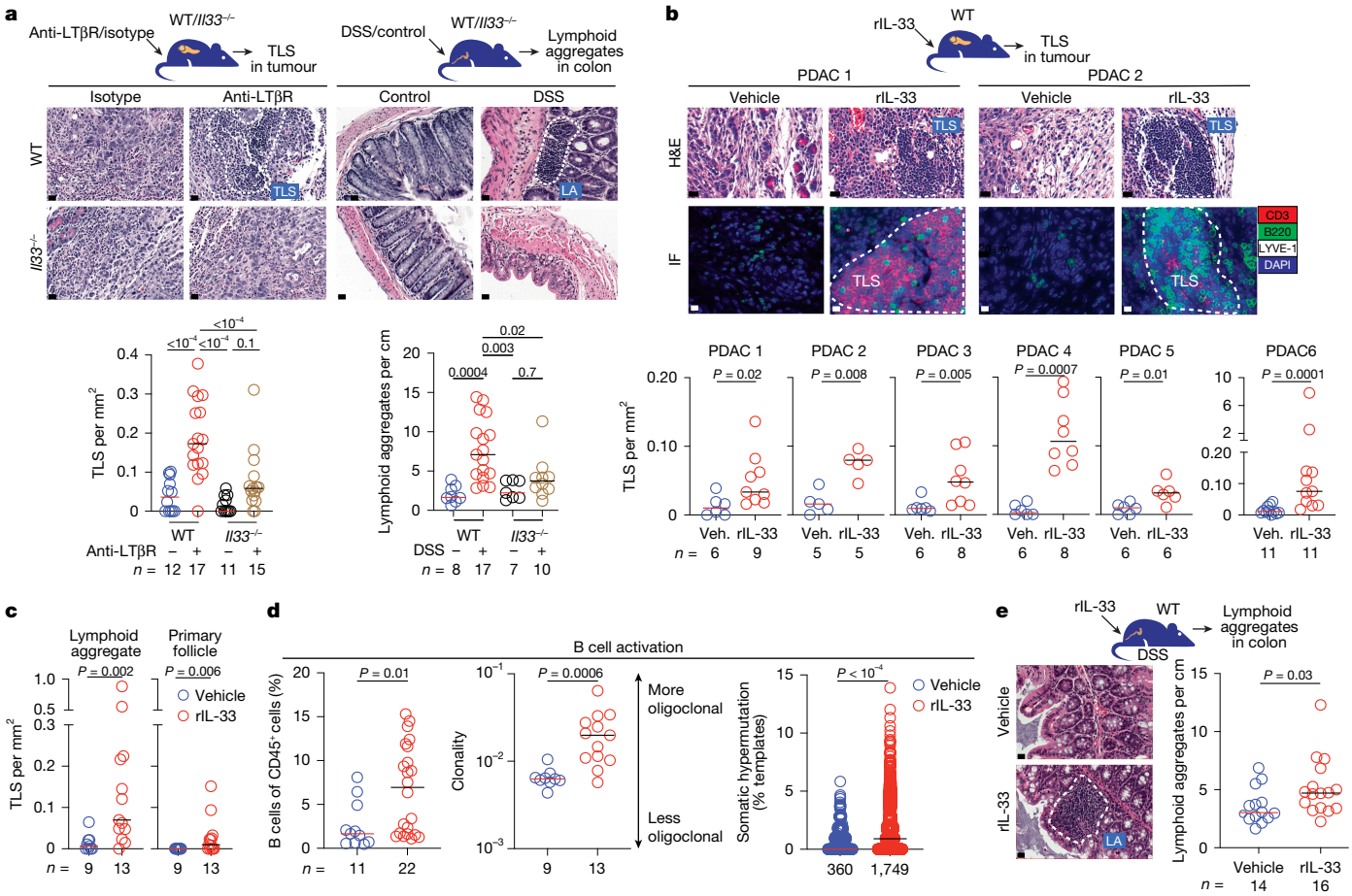

Fig. 2 | The alarmin domain of IL-33 induces TLSs in PDAC and chemical colitis. a, Haematoxylin and eosin staining (H&E) (top) and quantification of intratumoural TLSs (bottom left) and intracolonic lymphoid aggregates (LA; bottom right) in anti-LTβR-treated PDAC (left) and DSS-colitis (right) WT and *Il33*$^{-/-}$ mice. **b**, H&E (top) and immunofluorescence (IF; middle) staining, and the TLS density (H&E quantified; bottom) in vehicle (veh.) and rIL-33-treated PDAC mice. PDAC 1–6, orthotopic PDAC mice established with six PDAC cell lines. **c**,**d**, Intratumoural TLS maturation states (immunofluorescence quantified) (**c**), and the B cell frequency and clonality and somatic hypermutation (**d**) in vehicle-treated and rIL-33-treated PDAC mice. **e**, H&E and colonic LA quantification in vehicle-treated and rIL-33-treated DSS-colitis mice. Data were collected 2 weeks (**a**, left), 3 weeks (**b**, PDAC 3 and 4; **c** and **d**) and 3–5 weeks (**b**, PDAC 1, 2, 5 and 6) after tumour implantation, and 2 weeks after DSS initiation (**a** (right) and **e**), pooled from ≥2 independent experiments with $n \geq 2$ mice per group with consistent results. *n* represents the number of individual tumours or organs from individual mice analysed separately, or B cell clones (**d**, right). The dotted lines in **a**, **b** and **e** show putative TLS/LA; the horizontal bars in **a**–**e** show the median. *P* values were calculated using two-way analysis of variance (ANOVA) with Tukey's multiple-comparison test (**a**) and two-tailed Mann–Whitney *U*-test (**b**–**e**). Scale bars, 20 µm (**a**, **b** (top) and **e**) and 10 µm (**b** (bottom)).

Full-length IL-33 protein contains two domains—an N-terminal nuclear-localization domain and a C-terminal alarmin domain that, after tissue injury, is extracellularly cleaved to IL-33$_{109–266}$ and binds to the receptor ST2[10]. To probe whether IL-33 served as an inflammation-induced extracellular TLS trigger, we administered the alarmin domain of IL-33 (IL-33$_{109–266}$, hereafter, recombinant IL-33 (rIL-33)) to PDAC mice at doses (Extended Data Fig. 1e) that roughly approximated IL-33 steady-state levels in human sera of patients with PDAC (Extended Data Fig. 1f and Supplementary Table 3). rIL-33 induced de novo intratumoural TLSs across several TLS-poor, distinct cell-line-derived PDAC mouse models that spanned a range of intratumoural T cell infiltrates (Fig. 2b and Extended Data Fig. 2c,d). rIL-33 also induced different TLS maturation states, increasing the density of intratumoural lymphoid aggregates[15] (early TLS) and primary follicles[15] (intermediate TLS) in PDACs (Fig. 2c and Extended Data Fig. 2e). Moreover, tumours in rIL-33-treated PDAC mice evidenced TLSs with BCL6^{+} B cells (Extended Data Fig. 2f), and increased intratumoural B cell frequencies, B cell clonal expansion and somatic hypermutation[15] (Fig. 2d), suggesting germinal centre reactions and secondary follicle generation (late TLS)[15]. In DSS-colitis mice, rIL-33 expanded colonic lymphoid aggregates to a lesser degree (Fig. 2e), but attenuated weight loss and enhanced mouse survival (Extended Data Fig. 2g). Thus, the alarmin IL-33 triggers lymphoneogenesis in cancer and inflammation.

IL-33 expands lymphoneogenic ILC2s

As these results suggested an IL-33-driven lymphoneogenic pathway, we next sought to identify the cells that mediate rIL-33-induced TLSs. As we previously reported that rIL-33 dominantly expands intratumoural ST2^{+} ILC2s in PDAC mice[16], we examined the single-cell transcriptomes of ST2^{+} ILC2s in tumours and tumour draining lymph nodes (DLNs) in rIL-33-treated PDAC mice for lymphoneogenic molecules[16] (Fig. 3a). We detected an intratumoural population of ILC2s that co-expressed *Klrg1* and *Ltb* (Fig. 3a and Extended Data Fig. 3a,b), *Lta* (Extended Data Fig. 3b) and LT, the LTα1/β2 heterotrimeric cytokine essential for TLS neogenesis[1,11,13] (Fig. 3b and Extended Data Fig. 3c,d). Consistently, in multiple PDAC models and DSS-colitis mice, rIL-33 expanded intratumoural (Fig. 3c and Extended Data Fig. 3e) and gut (Fig. 3d) KLRG1^{+} ILC2s, but not KLRG1^{-} ILC2s, that expressed LT (Extended Data Fig. 3c,f). These rIL-33-induced intratumoural KLRG1^{+} ILC2s also expressed canonical ILC2 transcription factors (TFs) (*Gata3* and *Rora* (Fig. 3a and Extended

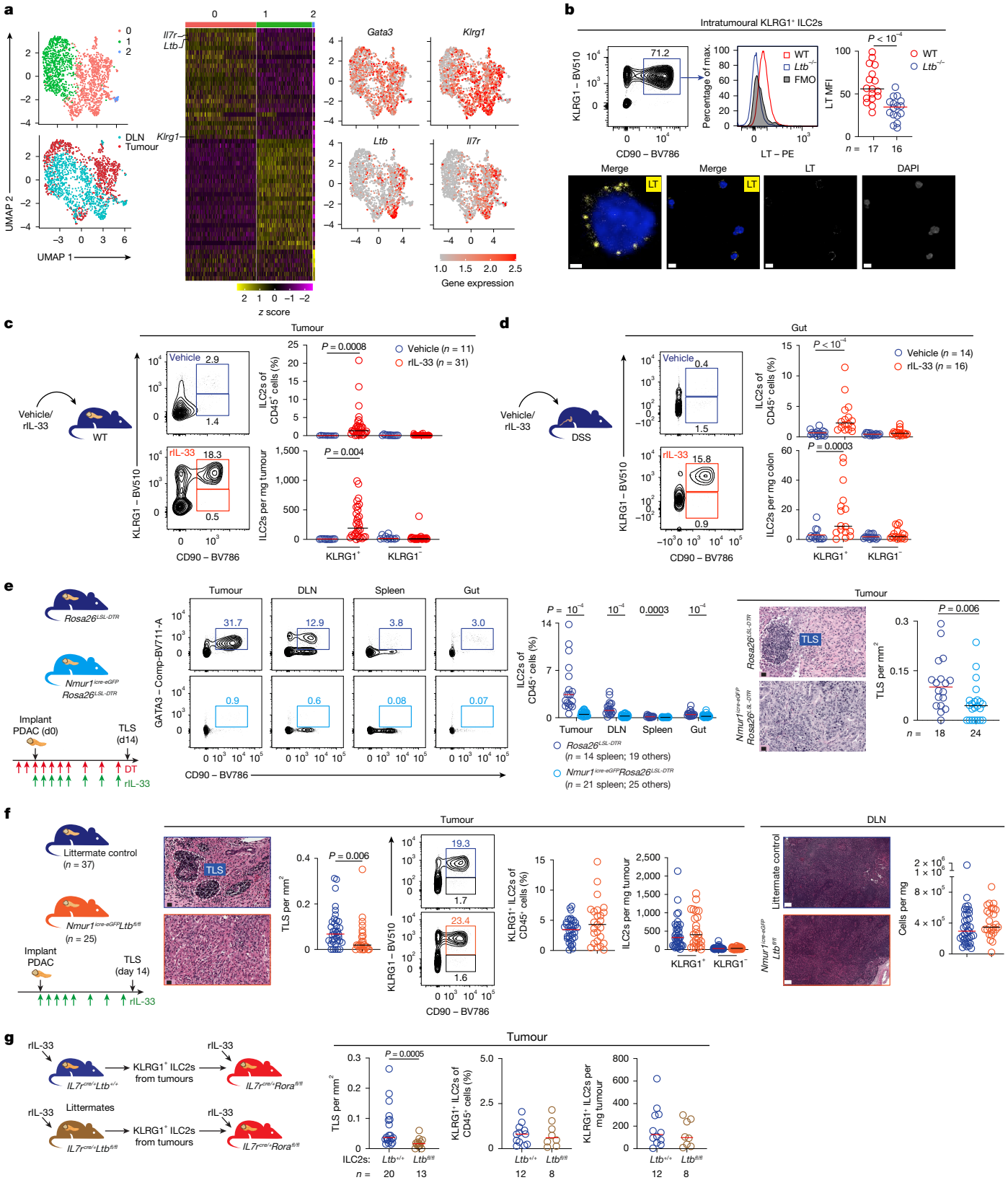

Fig. 3 | See next page for caption.

Data Fig. 3g–j) and *Id2* (Extended Data Fig. 3h)), cytokines (*Il5*, *Il13* and *Areg*; Extended Data Fig. 3h) and receptors (*Il7r* and *Nmur1*[17–19]; Fig. 3a and Extended Data Fig. 3i), but not ILC1 (*Tbx21* (encoding T-BET); Extended Data Fig. 3j) or ILC3 (*Rorc* (encoding RORγt); Extended Data Fig. 3h,j) TFs. Thus, rIL-33 expands KLRG1$^+$ ILC2s expressing LT that may mediate lymphoneogenesis.

Recent reports have revealed that ILC2s and precursors selectively express the neuromedin receptor (NMUR1) that can be used for

Fig. 3 | IL-33 activates lymphoneogenic ILC2s. a, Single-cell RNA-sequencing (scRNA-seq) analysis of purified tumour and DLN ILC2s from rIL-33-treated PDAC mice. The uniform manifold approximation and projection (UMAP) representations show cells by unsupervised clusters (top left), organs (bottom left) and select genes (right). The heat map (middle) shows the top 25 genes by cluster. The heat map scale bar represents the *z* score. The UMAP scale bar represents gene expression. **b**, Gating (left) and LT expression by flow cytometry (right) and confocal imaging (bottom) in intratumoural KLRG1$^+$ ILC2s from rIL-33-treated WT and *Ltb*$^{-/-}$ PDAC mice. FMO, fluorescence minus one; MFI, mean fluorescence intensity. **c**,**d**, Gating, and the frequency and number of intratumoural (**c**) and gut (**d**) ILC2s in vehicle-treated and rIL-33-treated PDAC (**c**) and DSS-colitis (**d**) mice. **e**, Gating (left), ILC2 frequency (middle) and intratumoural TLS density (right) in rIL-33 and DT-treated *Nmur1*$^{icre\text{-}eGFP}$*Rosa26*$^{LSL\text{-}DTR}$ and littermate control *Rosa26*$^{LSL\text{-}DTR}$ PDAC mice. **f**, Intratumoural TLS density (left), gating, frequency and the number of ILC2s, and the number of DLN immune cells (right) in rIL-33-treated *Nmur1*$^{icre\text{-}eGFP}$ *Ltb*$^{fl/fl}$ and littermate control PDAC mice. **g**, Tumour KLRG1$^+$ ILC2s were sort-purified from rIL-33-treated *Il7r*$^{cre/+}$*Ltb*$^{fl/fl}$ or *Il7r*$^{cre/+}$*Ltb*$^{+/+}$ littermate PDAC mice and transferred to *Il7r*$^{cre/+}$*Rora*$^{fl/fl}$ PDAC mouse recipients. The TLS density, KLRG1$^+$ ILC2 frequency and number in recipient PDACs. Data were collected at 10 days (**a**), 2 weeks (**b** and **d**–**f**) and 5 weeks (**c**) after tumour implantation, and 2 weeks (**g**) after transfer, pooled from ≥3 independent experiments with $n \geq 3$ mice per group with consistent results. *n* represents the number of individual tumours or organs from individual mice analysed separately. The horizontal bars show the median. In **f**, littermate controls include *Ltb*$^{fl/+}$ and *Nmur1*$^{icre\text{-}eGFP}$ *Ltb*$^{fl/+}$ combined. *P* values were calculated using two-tailed Mann–Whitney *U*-test (**b**, **e** (right), **f** and **g**) and two-way ANOVA with Holm's test (**c**, **d** and **e** (left)). Scale bars, 1 µm (**b** (left)), 5 µm (**b** (all others)), 20 µm (**e** and **f** (left)) and 100 µm (**f** (right)).

ILC2-specific genetic targeting[20,21]. To investigate whether ILC2s contribute to IL-33-mediated lymphoneogenesis, as ILC2s (but not other ILCs or immune cells) in our model also selectively expressed NMUR1 (Extended Data Fig. 4a), we used *Nmur1*$^{icre\text{-}eGFP}$*Rosa26*$^{LSL\text{-}DTR}$ transgenic mice[20] that constitutively express the human diphtheria toxin receptor (DTR) on NMUR1$^+$ cells to acutely and selectively deplete all ILC2s. In *Nmur1*$^{icre\text{-}eGFP}$*Rosa26*$^{LSL\text{-}DTR}$ PDAC mice, diphtheria toxin (DT) initiated 2 days before tumour implantation and rIL-33 treatment depleted ILC2s by approximately 85% within tumours and across organs (Fig. 3e (left)) while sparing ILC3s (Extended Data Fig. 4b) and other immune cells (Extended Data Fig. 4c). Notably, acute ILC2 depletion during rIL-33 treatment reduced intratumoural TLSs by approximately 65% (Fig. 3e (right)). Thus, ILC2s contribute to IL-33-mediated lymphoneogenesis.

Next, to examine whether ILC2s used cell-intrinsic LT to induce intratumoural TLSs, we generated transgenic mice that lack *Ltb* on ILC2s (*Nmur1*$^{icre\text{-}eGFP}$*Ltb*$^{fl/fl}$). In rIL-33-treated *Nmur1*$^{icre\text{-}eGFP}$*Ltb*$^{fl/fl}$ PDAC mice, compared with the littermate controls, ILC2-targeted *Ltb* deletion reduced intratumoural TLS density by approximately 70% without altering the frequencies of KLRG1$^+$ ILC2s (Fig. 3f), ILC1s, ILC3s and other immune cells in tumours (Extended Data Fig. 4d (top)), immune cells in DLNs (Fig. 3f (right)) or immune cell subsets in organs (Extended Data Fig. 4d (bottom)). Consistently, a broader genetic strategy to delete *Ltb* on all IL-7R$^+$ lymphocytes (*Il7r*$^{cre/+}$*Ltb*$^{fl/fl}$) also reduced intratumoural TLSs, but notably also reduced intratumoural KLRG1$^+$ ILC2s (Extended Data Fig. 4e), to suggest that non-ILC2 lymphocyte LT signalling may maximally expand KLRG1$^+$ ILC2s in tumours. rIL-33-treated *Il7r*$^{cre/+}$*Ltb*$^{fl/fl}$ PDAC mice also had comparable intratumoural frequencies of other immune cells but fewer eosinophils (Extended Data Fig. 4e (right)), consistent with the downstream effects of ILC2 depletion[20–22]. To confirm that ILC2s used LT to impact TLS formation using an orthogonal approach, we purified and transferred intratumoural KLRG1$^+$ ILC2s from rIL-33-treated *Il7r*$^{cre/+}$*Ltb*$^{fl/fl}$ or *Il7r*$^{cre/+}$*Ltb*$^{+/+}$ littermate PDAC mice[23] (that is, KLRG1$^+$ ILC2s proficient or deficient in *Ltb*) into *Il7r*$^{cre/+}$*Rora*$^{fl/fl}$ PDAC recipients that exhibit reduced peripheral ILC2s in tissues[24] (Fig. 3g). Compared with transferred ILC2s with intact *Ltb*, and consistent with the results in *Nmur1*$^{icre\text{-}eGFP}$*Ltb*$^{fl/fl}$ PDAC mice (Fig. 3f), ILC2-intrinsic *Ltb* deficiency reduced TLS formation without impairing rIL-33-mediated intratumoural KLRG1$^+$ ILC2 accumulation in tumours (Fig. 3g). Collectively, these molecular and cellular loss- and gain-of-function experiments suggest that rIL-33-activated KLRG1$^+$ ILC2s induce TLSs in PDACs using a pathway involving LT.

In SLOs and TLSs, inducer cells express LT that binds to LTβR on TLS organizer cells to stimulate the expression of chemokines and adhesion molecules, and coordinate lymphoneogenesis[3]. To identify the organizer cells that cooperate with rIL-33-induced KLRG1$^+$ ILC2s to induce TLSs in PDAC, we found that intratumoural CD11b$^+$ myeloid cells most highly expressed LTβR (Extended Data Fig. 5a). Compared with LTβR$^-$ myeloid cells, intratumoural LTβR$^+$ myeloid cells expressed a distinct transcriptome (Extended Data Fig. 5b–e and Supplementary Table 4), with higher TLS-inducing chemokines, including *Cxcl13*[25] and *Ccl19*[26] (Extended Data Fig. 5d), the canonical organizer cell adhesion molecule *Vcam1*[27] (Extended Data Fig. 5e) and inflammatory chemokines that recruit TLS cellular components[28–30] (Extended Data Fig. 5e). Intratumoural LTβR$^+$ myeloid cells also expressed *Il33* mRNA and protein (Extended Data Fig. 5f). Consistently, LTβR activation expanded intratumoural KLRG1$^+$ ILC2s in WT but not *Il33*$^{-/-}$ PDAC mice (Extended Data Fig. 5g) to indicate LTβR stimulation may expand KLRG1$^+$ ILC2s through an endogenous IL-33-dependent circuit. To test whether myeloid-cell-derived endogenous IL-33 modulated KLRG1$^+$ ILC2s in tumours, we purified IL-33 proficient (WT) or deficient (*Il33*$^{-/-}$) LTβR$^+$ myeloid cells from PDACs and co-implanted them with PDAC cells into pancreata of *Il33*$^{-/-}$ mice (Extended Data Fig. 5h). LTβR$^+$ myeloid-cell-derived IL-33 induced KLRG1$^+$ ILC2s in PDACs to express LT and induce TLSs (Extended Data Fig. 5h). Together, these data suggest that KLRG1$^+$ ILC2s and intratumoural myeloid cells cooperate as TLS inducer and organizer cells, respectively, to augment IL-33 signalling and induce TLSs in tumours.

Lymphoneogenic ILC2s can migrate from the gut

As our findings suggested a lymphoneogenic function for ILC2s, we investigated whether lymphoneogenic KLRG1$^+$ ILC2s expand locally or migrated to tumours[31]. In PDAC mice, as rIL-33 expanded KLRG1$^+$ ILC2s in the blood (Extended Data Fig. 6a), we used congenic parabiotic mice with PDACs in recipient pancreata to test whether KLRG1$^+$ ILC2s migrated haematogenously to tumours (Extended Data Fig. 6b). rIL-33 administered to donor parabionts induced donor KLRG1$^+$ (Fig. 4a) but not KLRG1$^-$ ILC2s or non-ILCs (Extended Data Fig. 6c,d) to migrate to recipient parabiont blood and tumours. Thus, KLRG1$^+$ ILC2s migrate haematogenously to tumours.

As ILC2s can migrate to tissues from the gut[32], we hypothesized that the gut might be one source of KLRG1$^+$ ILC2s that migrate to pancreatic tumours. To trace the origin of intratumoural KLRG1$^+$ ILC2s, we used KikGR transgenic mice in which all cells express a green-to-red photoconvertible protein. We treated KikGR PDAC mice with rIL-33, photoconverted gut tissue and searched for gut-derived red KLRG1$^+$ ILC2s in PDACs (Fig. 4b). In rIL-33-treated PDAC mice, we detected rare red KLRG1$^+$ ILC2s in tumours of gut-photoconverted but not control (sham treated; peritoneum-photoconverted) mice (Fig. 4b and Extended Data Fig. 6e), indicating that KLRG1$^+$ ILC2s can migrate to PDACs through a gut–blood circuit.

To examine whether PDACs primed such a gut-derived migratory ILC2 circuit, we searched for gut-derived signals that may stimulate ILC2s to migrate. As recent findings indicate gut microbiota can stimulate ILC2s to migrate in acute inflammatory states[33], we examined whether PDACs altered gut microbiota and, consequently, stimulated gut ILC2

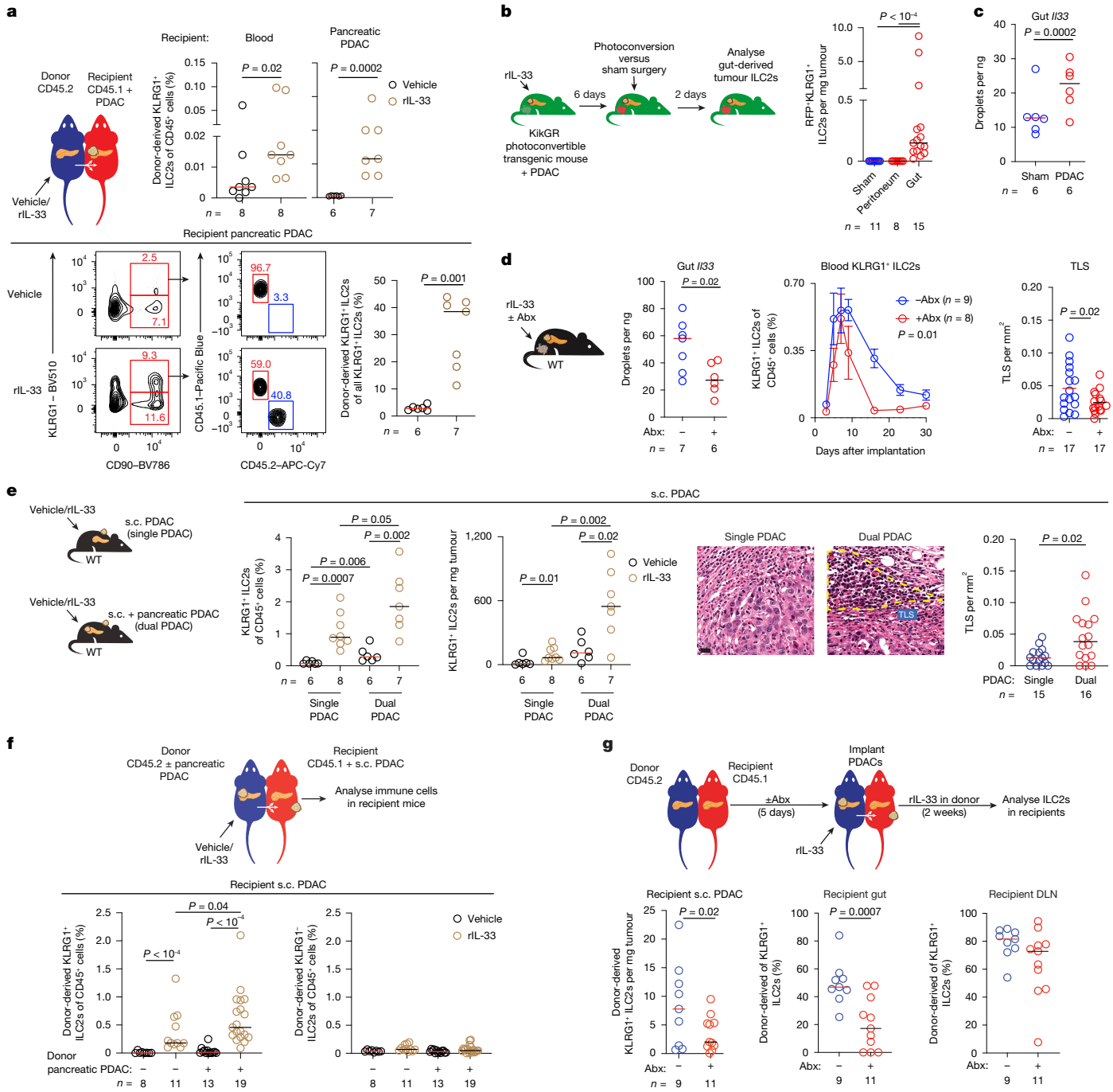

Fig. 4 | Lymphoneogenic ILC2s migrate to tumours through a microbiota- and PDAC-modulated gut–blood circuit. a, Parabiotic mice with PDACs in recipient pancreata. Donors were treated with vehicle or rIL-33. Quantification (top) and gating (bottom) of donor-derived ILC2s in recipient blood and PDAC. **b**, KikGR PDAC mice were treated daily with rIL-33 for 6 days. On day 6, the gut or peritoneum was photoconverted. Experimental schematic (left) and density of gut-derived (RFP^+) ILC2s in pancreatic PDACs (right). **c**, Gut *Il33* mRNA was analysed by digital droplet PCR in sham-treated and PDAC mice. **d**, Gut *Il33* mRNA (left), blood $KLRG1^+$ ILC2s (middle) and the intratumoural TLS density (right) in rIL-33-treated PDAC mice treated with or without antibiotics (Abx). **e**, The intratumoural $KLRG1^+$ ILC2 frequency, number and TLS density in skin (s.c.) PDACs in vehicle-treated and rIL-33-treated mice with s.c. alone (single PDAC) or s.c. and pancreatic PDACs (dual PDAC). **f**, Parabiotic mice with s.c. PDACs in recipients with or without pancreatic PDACs in donors. Donors were treated with vehicle or rIL-33. The donor-derived ILC2 frequency in recipient s.c. PDACs (bottom) is shown. **g**, Parabiotic mice with s.c. PDACs in recipients and pancreatic PDACs in donors. Donors were treated with rIL-33; donor and recipients were treated with antibiotics. The donor-derived ILC2 number and frequency in recipient s.c. PDACs and gut (bottom) are shown. Data were collected at 2 weeks (**a**, **e** (left), **f** and **g**), as shown in the experimental schema (**b**), 4 weeks (**c** and **d**) and 5 weeks (**e** (right)) after tumour implantation, pooled from ≥2 independent experiments with $n \geq 3$ mice per group with consistent results. *n* values represent the number of individual tumours or organs from individual mice analysed separately. The horizontal bars show the median. *P* values were calculated using two-tailed Mann–Whitney *U*-test (**a**, **c**, **d**, **e** (right) and **g**), one-way ANOVA with Kruskal–Wallis multiple-comparison test (**b**), two-way ANOVA with Kruskal–Wallis test (**d**, middle) and two-way ANOVA with Sidak's multiple-comparison test (**e** (left) and **f**). Scale bar, 20 µm (**e**).

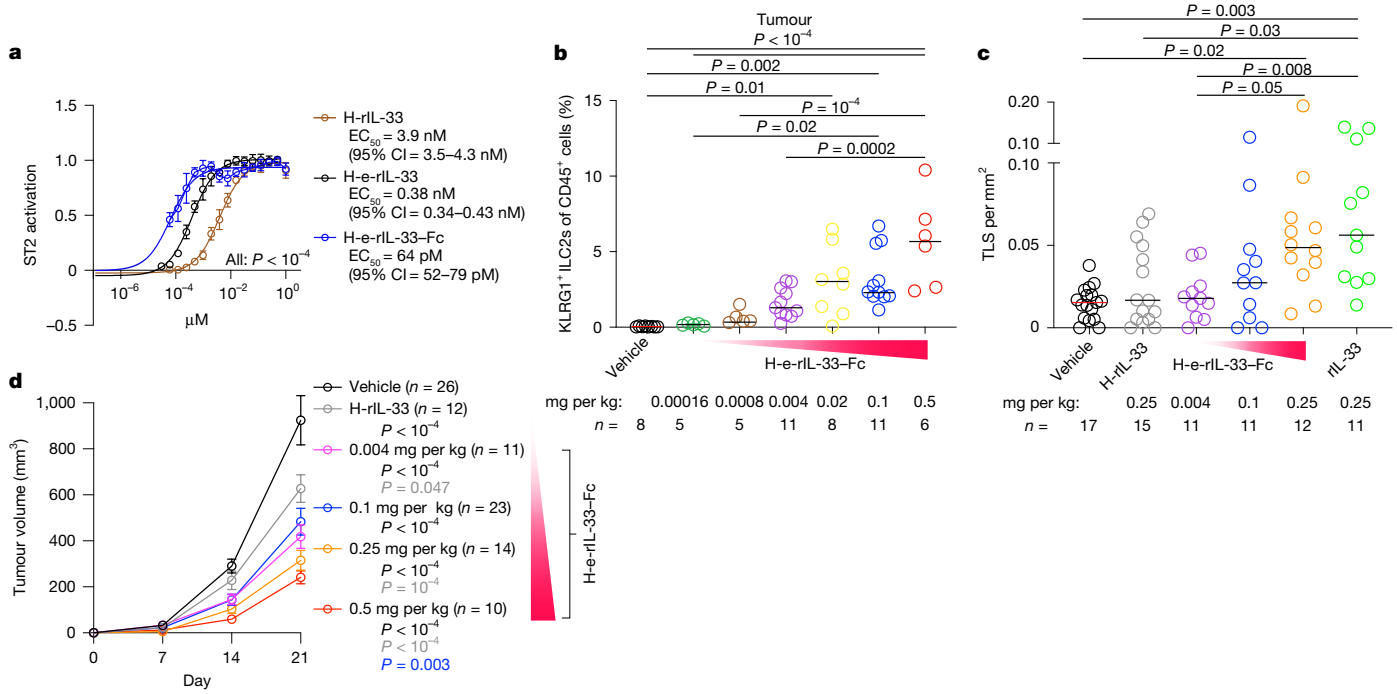

Fig. 5 | An engineered human IL-33 therapeutic stimulates TLSs and anti-tumour activity in PDAC. a, ST2 activation in HEK blue human IL-33 reporter cells with H-rIL-33, H-e-rIL-33 and H-e-rIL-33–Fc. EC_{50}, half-maximal effective concentration. **b**–**d**, The intratumoural KLRG1$^+$ ILC2 frequency (**b**), TLS density (**c**) and tumour volume (**d**) in PDAC mice treated with vehicle, mouse rIL-33, H-rIL-33 or escalating H-e-rIL-33–Fc. Curves in **a** were fit by nonlinear regression. Data were collected at 3–4 weeks (**b** and **c**) after tumour implantation, pooled from ≥2 independent experiments with $n \geq 3$ mice per group with consistent results. *n* values represent the number of individual tumours from individual mice. The horizontal bars show the median. *P* values were calculated using extra-sum-of-squares *F* test (**a**) and two-way ANOVA with Tukey's multiple-comparison correction test (**b**–**d**).

reservoirs[34]. Notably, PDACs not only increased intrapancreatic KLRG1$^+$ ILC2 frequencies (Extended Data Fig. 7a), but also increased the diversity and altered the composition of gut microbiota (Extended Data Fig. 7b) and increased gut *Il33* mRNA expression (Fig. 4c), suggesting that gut microbial changes may increase gut IL-33 levels and stimulate gut KLRG1$^+$ ILC2s to migrate[35]. Consistently, antibiotic-mediated microbiota ablation[36] decreased gut *Il33* mRNA expression, decreased the frequency of blood KLRG1$^+$ ILC2s and reduced intratumoural TLSs (Fig. 4d). Furthermore, microbiota ablation slightly reduced serum IL-33, and reciprocally increased the frequency of gut KLRG1$^+$ ILC2s (Extended Data Fig. 7c) that, consistently, was reduced after microbiota restoration in germ-free mice (Extended Data Fig. 7d), suggesting that microbiota composition may modulate the ability of gut KLRG1$^+$ ILC2s to enter the circulation. Collectively, these results suggest that KLRG1$^+$ ILC2s can migrate to tumours from the gut and are modulated by gut microbiota.

As these results suggest PDACs prime the host to extrude ILC2s to inflamed sites, we investigated whether PDACs could amplify the ILC2 response to tumours in distant tissues. To test this, we administered rIL-33 to mice with either single (skin alone, subcutaneous (s.c.) PDAC) or dual (s.c. and pancreatic) PDACs. In contrast to single-PDAC mice, in which rIL-33 expanded intratumoural KLRG1$^+$ ILC2s yet did not control s.c. PDAC growth, in dual-PDAC mice, rIL-33 further amplified KLRG1$^+$ ILC2 frequencies, boosted TLS densities (Fig. 4e) and controlled tumour growth in s.c. PDACs (Extended Data Fig. 8a). To confirm that dual-PDACs amplified KLRG1$^+$ ILC2s that trafficked haematogenously to s.c. tumours, we modelled dual PDACs in parabiotic mice with pancreatic PDACs in donor parabionts and s.c. PDACs in recipients (Fig. 4f). Consistent with the findings in dual-PDAC mice, pancreatic PDACs in donor parabionts increased rIL-33-induced KLRG1$^+$ but not KLRG1$^-$ ILC2 migration to s.c. PDACs in recipient parabionts (Fig. 4f and Extended Data Fig. 8b). This pancreatic PDAC-amplified haematogenous KLRG1$^+$ ILC2 trafficking to s.c. PDACs required distinct cytokines compared to acute infections as, although both rIL-33 and rIL-25 expanded KLRG1$^+$ ILC2s in donor PDACs (Extended Data Fig. 8c), only rIL-33[35] and not rIL-25[31] disseminated KLRG1$^+$ ILC2s from donor parabionts into recipient parabiont blood and s.c. PDACs (Extended Data Fig. 8c). Furthermore, increased migration to s.c. PDACs in dual-PDAC mice was accompanied by restricted s.c. PDAC growth in an ST2-, LTβR-, *Ltb*- and *Rora*-dependent manner (Extended Data Fig. 8d–g). Finally, microbiota ablation in parabiotic PDAC mice decreased donor-derived ILC2s in recipient s.c. PDACs and gut, but not recipient DLNs (Fig. 4g and Extended Data Fig. 8h), indicating that microbiota amplify KLRG1$^+$ ILC2s in tumours connected to a gut–blood circuit. In summary, a host pancreatic PDAC amplifies microbiota-mediated haematogenous ILC2 migration to PDACs in distant tissues.

Engineered IL-33 amplifies lymphoneogenesis

To examine the relevance of our findings in humans, we next investigated whether LT-expressing KLRG1$^+$ ILC2s are present in human cancer. In human PDACs, we detected KLRG1$^+$ ILC2s that expressed LT (Extended Data Fig. 9a–c and Supplementary Table 5), suggesting that KLRG1$^+$ ILC2s may exert similar lymphoneogenic function in human tumours. To investigate the association between IL-33-activated ILC2s and intratumoural TLSs, we developed a human transcriptional signature of rIL-33-activated ILC2s (Methods) and examined its association with TLS signatures[4,7,8] in tumours spanning a spectrum of immune activity ($n = 12$ histologies, 4,037 tumours). Activated ILC2 signatures correlated with all three TLS transcriptional signatures (Extended Data Fig. 1g), suggesting that KLRG1$^+$ ILC2s may contribute to TLS formation in human tumours.

As the presence of KLRG1$^+$ ILC2s in human tumours suggested that the IL-33–ILC2–TLS pathway could be manipulated for immunotherapy, we engineered human rIL-33 (H-rIL-33) to increase its activity and half-life in vivo. First, to eliminate cysteine oxidation that triggers disulfide

bonding and conformational changes that disrupt the ST2-binding site of IL-33, we substituted all four cysteine residues in human IL-$33_{112–270}$ to serine residues[37] (hereafter, H-enhanced-rIL-33 (H-e-rIL-33)). We found that H-e-rIL-33 enhanced ST2 activation compared with H-rIL-33, consistent with previous observations[37] (Fig. 5a). Next, to prolong the H-e-rIL-33 half-life in vivo, we used an established approach[38] and fused H-e-rIL-33 to the human IgG1 Fc fragment (H-e-rIL-33–Fc) with described L234A/L235A substitutions that limit Fc gamma receptor binding through a short Gly/Ser-containing linker. We then confirmed that H-e-rIL-33–Fc enhanced in vitro ST2 activation compared with H-rIL-33 and H-e-rIL-33 (Fig. 5a). As numerous studies have shown that human IL-33 is biologically active in mice[39], we tested whether H-e-rIL-33–Fc expanded KLRG1$^+$ ILC2s and induced TLSs in mice. Consistently, H-e-rIL-33–Fc expanded intratumoural KLRG1$^+$ ILC2s and TLSs in a dose-dependent manner (Fig. 5b,c) to control PDAC tumours (Fig. 5d). Thus, the IL-33–ILC2–TLS axis is a previously undescribed pathway that can be engineered to treat pancreatic cancer (Extended Data Fig. 10).

Discussion

We find that IL-33, an alarmin that is canonically released by damaged tissues, activates a migratory cellular lymphoneogenic response. Such a pathway may have been predictable in hindsight—lymphoid tissue inducer cells, the cells that initiate prenatal lymphoid organogenesis, contract in the postnatal adult[40]. Although ILC3s may subsume some lymphoneogenic lymphoid tissue inducer function in adults[41], ILC3s do not canonically respond to damage signals. Thus, one may hypothesize that a non-redundant cellular pathway must initiate lymphoneogenesis in response to tissue injury. Indeed, our findings highlight IL-33 as a candidate inflammatory TLS initiator, and ILC2s as a candidate inducer, of such a pathway.

Our observations do not imply ILC2s are the sole inducers of IL-33-driven lymphoneogenesis. Although gain- and loss-of-function studies demonstrate ILC2s indeed induce TLSs in an LT-dependent manner, our results do not exclude that IL-33-driven TLSs may harness contributions from other ST2$^+$ cells, including activated T cells[42] and B cells[14] that respond to IL-33[14,42]. Moreover, IL-33 may also activate other immune[43] and non-immune[44] cells to exert both anti- and, possibly, pro-neoplastic effects in different contexts through non-TLS mechanisms. As *Nmur1* is expressed in the nervous system[45], our genetic strategy to selectively deplete ILC2s by targeting *Nmur1* with DT may confound attempts to study TLS formation in neuronal tissues. Yet, as ILC2s respond early to tissue damage and recruit other lymphocytes to injured sites, ILC2s are prime candidate apex cells to initiate IL-33-driven TLSs and amplify the TLS response[16]. This broadens the scope of the recognized alarmin function of IL-33, and the role of ILC2s as sentinels of injury, to include inflammation-triggered lymphoneogenesis.

The fidelity of such a mobile lymphogenic pathway is further supported by companion intratumoural myeloid cells that appear to cooperatively generate TLSs. Indeed, myeloid cells and other immune cells inducibly express IL-33[46] and LTβR[47], and release cytosolic IL-33[48] (not demonstrated in our study) through a translocation pathway for leaderless proteins[49] that lack a secretory signal peptide. Yet, why myeloid cells possess the molecular machinery to express IL-33 has remained unclear. We posit that myeloid cells may use IL-33 to feedback and sustain LT expression to ensure continuous local levels of IL-33. Thus, IL-33 may be expressed in myeloid cells to both expand inducer cells in injured tissues to initiate TLSs and enable organizer cells to further amplify this response. Although we find that myeloid cells use IL-33 to induce LT on ILC2s, this pathway may extend to other IL-33- and LT-expressing cells. Notably, as we do not demonstrate that myeloid cells secrete IL-33, we cannot rule out that the N-terminal domain may also contribute to lymphoneogenesis. Yet, these findings—self-sustained expression of the inducing ligand through a cellular and molecular feedback loop—bear the hallmark of a novel TLS pathway. Physiologically, this organizational structure would logically preprogram SLOs at defined anatomical locations and equip migratory cells with molecular machinery to traffic to tissues to induce TLSs.

Our finding that PDAC primes this host lymphoneogenic response from the gut and is modulated by microbiota is notable, as a precise understanding of cells that link gut microbiota to both TLSs and tumour immunity remains in evolution. However, we did not investigate, and therefore cannot rule out, the functional contributions of ILC2s migrating to tumours from other sources, or of non-migratory ILC2s. Thus, as circulating ILC2s can derive from different tissue reservoirs[34], ILC2s may plausibly migrate to tumours not only from the gut but also from alternative reservoirs to generate a coordinated host response to a tumour. Notwithstanding, our findings introduce ILC2s as potential cells through which microbiota may modulate tumour immunity.

The ability to engineer the IL-33–ST2 pathway to boost TLSs and potentially control PDAC could have implications for cancer immunotherapy. As PDAC phenocopies the approximately 80% of immunologically cold tumours that appear to be insufficiently immunogenic and therefore insensitive to first-generation immunotherapies that amplify endogenous immunity, strategies to boost TLSs in PDAC could unlock pathways to activate immunity in other cancers, either as monotherapy or in combination with other activating strategies. Yet, as the role of IL-33 in cancer appears multifaceted (for example, full-length IL-33 expressed in cancer cells may accelerate tumour growth[44,50] in contrast to selective delivery of the ST2-binding domain of IL-33 as shown here) and in evolution, clinical translation will require rational application. Although we activate this pathway, one also envisions blocking this pathway to treat chronic inflammatory diseases mediated by excess TLS activity. Regardless, our findings more broadly suggest that alarmin-triggered lymphoneogenesis can be harnessed for immunotherapy.

Online content

Any methods, additional references, Nature Portfolio reporting summaries, source data, extended data, supplementary information, acknowledgements, peer review information; details of author contributions and competing interests; and statements of data and code availability are available at https://doi.org/10.1038/s41586-024-08426-5.

1. Kratz, A., Campos-Neto, A., Hanson, M. S. & Ruddle, N. H. Chronic inflammation caused by lymphotoxin is lymphoid neogenesis. *J. Exp. Med.* **183**, 1461–1472 (1996).
2. Scott, I. C. et al. Interleukin-33 is activated by allergen- and necrosis-associated proteolytic activities to regulate its alarmin activity during epithelial damage. *Sci. Rep.* **8**, 3363 (2018).
3. Sautès-Fridman, C., Petitprez, F., Calderaro, J. & Fridman, W. H. Tertiary lymphoid structures in the era of cancer immunotherapy. *Nat. Rev. Cancer* **19**, 307–325 (2019).
4. Cabrita, R. et al. Tertiary lymphoid structures improve immunotherapy and survival in melanoma. *Nature* **577**, 561–565 (2020).
5. Petitprez, F. et al. B cells are associated with survival and immunotherapy response in sarcoma. *Nature* **577**, 556–560 (2020).
6. Helmink, B. A. et al. B cells and tertiary lymphoid structures promote immunotherapy response. *Nature* **577**, 549–555 (2020).
7. Coppola, D. et al. Unique ectopic lymph node-like structures present in human primary colorectal carcinoma are identified by immune gene array profiling. *Am. J. Pathol.* **179**, 37–45 (2011).
8. Gu-Trantien, C. et al. CD4$^+$ follicular helper T cell infiltration predicts breast cancer survival. *J. Clin. Invest.* **123**, 2873–2892 (2013).
9. Hiraoka, N. et al. Intratumoral tertiary lymphoid organ is a favourable prognosticator in patients with pancreatic cancer. *Br. J. Cancer* **112**, 1782–1790 (2015).
10. Liew, F. Y., Girard, J.-P. & Turnquist, H. R. Interleukin-33 in health and disease. *Nat. Rev. Immunol.* **16**, 676–689 (2016).
11. Drayton, D. L., Ying, X., Lee, J., Lesslauer, W. & Ruddle, N. H. Ectopic LTαβ directs lymphoid organ neogenesis with concomitant expression of peripheral node addressin and a HEV-restricted sulfotransferase. *J. Exp. Med.* **197**, 1153–1163 (2003).
12. Lukashev, M. et al. Targeting the lymphotoxin-β receptor with agonist antibodies as a potential cancer therapy. *Cancer Res.* **66**, 9617–9624 (2006).
13. Rennert, P. D., James, D., Mackay, F., Browning, J. L. & Hochman, P. S. Lymph node genesis is induced by signaling through the lymphotoxin β receptor. *Immunity* **9**, 71–79 (1998).
14. Lochner, M. et al. Microbiota-induced tertiary lymphoid tissues aggravate inflammatory disease in the absence of RORγt and LTi cells. *J. Exp. Med.* **208**, 125–134 (2010).
15. Schumacher, T. N. & Thommen, D. S. Tertiary lymphoid structures in cancer. *Science* **375**, eabf9419 (2022).

16. Moral, J. A. et al. ILC2s amplify PD-1 blockade by activating tissue-specific cancer immunity. *Nature* **579**, 790–796 (2020).
17. Klose, C. S. N. et al. The neuropeptide neuromedin U stimulates innate lymphoid cells and type 2 inflammation. *Nature* **549**, 282–286 (2017).
18. Wallrapp, A. et al. The neuropeptide NMU amplifies ILC2-driven allergic lung inflammation. *Nature* **549**, 351–356 (2017).
19. Cardoso, V. et al. Neuronal regulation of type 2 innate lymphoid cells via neuromedin U. *Nature* **549**, 277–281 (2017).
20. Tsou, A. M. et al. Neuropeptide regulation of non-redundant ILC2 responses at barrier surfaces. *Nature* **611**, 787–793 (2022).
21. Jarick, K. J. et al. Non-redundant functions of group 2 innate lymphoid cells. *Nature* **611**, 794–800 (2022).
22. Nussbaum, J. C. et al. Type 2 innate lymphoid cells control eosinophil homeostasis. *Nature* **502**, 245–248 (2013).
23. Gogoi, M. et al. ILC2-derived LIF licences progress from tissue to systemic immunity. *Nature* **632**, 885–892 (2024).
24. Oliphant, C. J. et al. MHCII-mediated dialog between group 2 innate lymphoid cells and $CD4^+$ T cells potentiates type 2 immunity and promotes parasitic helminth expulsion. *Immunity* **41**, 283–295 (2014).
25. Ansel, K. M. et al. A chemokine-driven positive feedback loop organizes lymphoid follicles. *Nature* **406**, 309–314 (2000).
26. Luther, S. A. et al. Differing activities of homeostatic chemokines CCL19, CCL21, and CXCL12 in lymphocyte and dendritic cell recruitment and lymphoid neogenesis. *J. Immunol.* **169**, 424–433 (2002).
27. Meier, D. et al. Ectopic lymphoid-organ development occurs through interleukin 7-mediated enhanced survival of lymphoid-tissue-inducer cells. *Immunity* **26**, 643–654 (2007).
28. Sarafi, M. N., Garcia-Zepeda, E. A., MacLean, J. A., Charo, I. F. & Luster, A. D. Murine monocyte chemoattractant protein (MCP)-5: a novel CC chemokine that is a structural and functional homologue of human MCP-1. *J. Exp. Med.* **185**, 99–110 (1997).
29. Zhao, X. et al. CCL9 is secreted by the follicle-associated epithelium and recruits dome region Peyer's patch $CD11b^+$ dendritic cells. *J. Immunol.* **171**, 2797–2803 (2003).
30. Zhang, M. et al. CCL7 recruits cDC1 to promote antitumor immunity and facilitate checkpoint immunotherapy to non-small cell lung cancer. *Nat. Commun.* **11**, 6119 (2020).
31. Huang, Y. et al. IL-25-responsive, lineage-negative KLRG1(hi) cells are multipotential "inflammatory" type 2 innate lymphoid cells. *Nat. Immunol.* **16**, 161–169 (2015).
32. Huang, Y. et al. S1P-dependent interorgan trafficking of group 2 innate lymphoid cells supports host defense. *Science* **359**, 114–119 (2018).
33. Pu, Q. et al. Gut microbiota regulate gut–lung axis inflammatory responses by mediating ILC2 compartmental migration. *J. Immunol.* **207**, 257–267 (2021).
34. Ricardo-Gonzalez, R. R. et al. Tissue-specific pathways extrude activated ILC2s to disseminate type 2 immunity. *J. Exp. Med.* **217**, 171 (2020).
35. Flamar, A.-L. et al. Interleukin-33 induces the enzyme tryptophan hydroxylase 1 to promote inflammatory group 2 innate lymphoid cell-mediated immunity. *Immunity* https://doi.org/10.1016/j.immuni.2020.02.009 (2020).
36. Pushalkar, S. et al. The pancreatic cancer microbiome promotes oncogenesis by induction of innate and adaptive immune suppression. *Cancer Discov.* **8**, 403–416 (2018).
37. Cohen, E. S. et al. Oxidation of the alarmin IL-33 regulates ST2-dependent inflammation. *Nat. Commun.* **6**, 1–10 (2015).
38. Alt, C. et al. Long-acting IL-33 mobilizes high-quality hematopoietic stem and progenitor cells more efficiently than granulocyte colony-stimulating factor or AMD3100. *Biol. Blood Marrow Transplant* **25**, 1475–1485 (2019).
39. Schmitz, J. et al. IL-33, an interleukin-1-like cytokine that signals via the IL-1 receptor-related protein ST2 and induces T helper type 2-associated cytokines. *Immunity* **23**, 479–490 (2005).
40. Sawa, S. et al. Lineage relationship analysis of $ROR\gamma t^+$ innate lymphoid cells. *Science* **330**, 665–669 (2010).
41. Ikeda, A. et al. Human $NKp44^+$ group 3 innate lymphoid cells associate with tumor-associated tertiary lymphoid structures in colorectal cancer. *Cancer Immunol. Res.* **8**, 724–731 (2020).
42. Peters, A. et al. Th17 cells induce ectopic lymphoid follicles in central nervous system tissue inflammation. *Immunity* **35**, 986–996 (2011).
43. Jacquelot, N. et al. Blockade of the co-inhibitory molecule PD-1 unleashes ILC2-dependent antitumor immunity in melanoma. *Nat. Immunol.* https://doi.org/10.1038/s41590-021-00943-z (2021).
44. Alonso-Curbelo, D. et al. A gene–environment-induced epigenetic program initiates tumorigenesis. *Nature* **590**, 642–648 (2021).
45. Howard, A. D. et al. Identification of receptors for neuromedin U and its role in feeding. *Nature* **406**, 70–74 (2000).
46. Qi, F. et al. Macrophages produce IL-33 by activating MAPK signaling pathway during RSV infection. *Mol. Immunol.* **87**, 284–292 (2017).
47. Kabashima, K. et al. Intrinsic lymphotoxin-beta receptor requirement for homeostasis of lymphoid tissue dendritic cells. *Immunity* **22**, 439–450 (2005).
48. Hung, L.-Y. et al. Cellular context of IL-33 expression dictates impact on anti-helminth immunity. *Sci. Immunol.* **5**, eabc6259 (2020).
49. Zhang, M. et al. A translocation pathway for vesicle-mediated unconventional protein secretion. *Cell* **181**, 637–652.e15 (2020).
50. Alam, A. et al. Fungal mycobiome drives IL-33 secretion and type 2 immunity in pancreatic cancer. *Cancer Cell* **40**, 153–167.e11 (2022).

Methods

Mice

C57BL/6 (WT, CD45.2) and C57BL/6 CD45.1 mice were purchased from Jackson Laboratory. *Il1rl1*$^{-/-}$ (ST2 deficient) and *Il33*$^{-/-}$ mice were a gift from M. J. Rosen. *Ltb*$^{fl/fl}$ mice and *Ltbr*$^{-/-}$ mice were previously described[51,52]. *Il7r*$^{cre/+}$*Rora*$^{fl/fl}$ mice were a gift from A. N. J. McKenzie. *Nmur1*$^{icre\text{-}eGFP}$*Rosa*$^{LSL\text{-}DTR}$ mice were previously described[20]. *Ltb*$^{fl/fl}$ mice were crossed to *Nmur1*$^{icre\text{-}eGFP}$ and *Il7r*$^{cre/+}$ mice to obtain *Nmur1*$^{icre\text{-}iGFP}$*Ltb*$^{fl/fl}$ and *Il7r*$^{cre/+}$*Ltb*$^{fl/fl}$ mice. *CAG-KikGR*[53] mice were a gift from G. E. Diehl. Germ-free mice were provided by the gnotobiotic facility at Weill Cornell Medical Center. For all experiments, 6–14-week-old mice were age and sex matched and randomly assigned to specified treatment groups, with at least two independent experiments performed throughout. Sample sizes for experiments were determined without formal power calculations. Animals were bred and maintained in a specific-pathogen-free animal facility. All experiments were conducted in accordance with an Institutional Animal Care and Use Committee (IACUC) approved protocol at Memorial Sloan Kettering Cancer Center (MSK) and in compliance with all IACUC-relevant ethical regulations.

Cell lines and animal procedures

Cell lines. All tumour cell lines (gifts from R. H. Vonderheide and B. J Stanger) were derived from KPC (*Pdx1-cre;LSL-Kras*$^{G12D/+}$;*LSL-Trp53*$^{R172H/+}$) or KPCY (*Pdx1-cre;LSL-Kras*$^{G12D/+}$;*LSL-Trp53*$^{R172H/+}$;*Rosa26*$^{YFP/YFP}$) mice. All cell lines were authenticated as bona fide PDAC cell lines based on histopathological verification by a dedicated pancreatic cancer pathologist. The HEK-Blue-IL-33 cell line (Invivogen) was cultured in DMEM (Gibco), 10% FBS (Gibco), penicillin (100 IU ml^{-1}), streptomycin (100 μg ml^{-1}) and 100 μg ml^{-1} normocin (Invivogen) at 37 °C in 5% CO_2. All of the other cell lines were cultured in DMEM with 10% FBS and glutamine (2 mM) at 37 °C in 5% CO_2. All of the cell lines were regularly tested using the MycoAlert Mycoplasma Detection Kit (Lonza).

PDAC tumours. Tumours were implanted orthotopically (pancreatic, PDAC mice) or s.c. as previously described[16]. In brief, for orthotopic implantation, mice were anaesthetized using isoflurane, and a small (7 mm) left abdominal side incision was made. Tumour cells (10^6 cells for KPC-4662 (PDAC 6); 10^5 cells for all others) were suspended in Matrigel (Becton Dickinson), diluted 1:1 with cold PBS, and injected as a 50 μl volume into the tail of the pancreas with a 31-gauge needle. Successful injection was verified by the appearance of a fluid bubble without intraperitoneal (i.p.) leakage. The abdominal wall was closed with absorbable PDS-II sutures (Ethicon), and the skin was closed with wound clips (Roboz). For s.c. implantation, tumour cells (5×10^5 cells for KPC-4662 (PDAC 6); 5×10^4 cells for all others) were resuspended in sterile PBS and implanted s.c. All tumours (PDAC and s.c.) were established with KPC-4662 (PDAC 6) unless otherwise specified. For sham surgery, mice were treated with orthotopic Matrigel injections only.

In PDAC mice, tumour volumes were measured using serial ultrasound (Vevo 2100 microultrasound, Visual Sonics) and analysed (Vivo Lab v.3.1.1, Fuji Film Visual Sonics) as previously described[16]. Tumours were collected at the indicated timepoints. To assess T cell infiltrates in PDACs derived from different cell lines (Extended Data Fig. 2c), tumours were collected at timepoints with comparable volumes. For s.c. tumours, tumour length and width were measured every 2–3 days with callipers, and tumour volumes were calculated as volume = (length/2) × width^2. Mice were euthanized at the indicated timepoints and processed for histology or flow cytometry. No blinding was performed in experimental mouse interventions, as knowledge of the treatment groups was required. For survival analyses, survival was determined by a tumour volume of ≥500 mm^3 or mouse health requiring euthanasia as defined by institutional IACUC guidelines. No mouse tumours exceeded IACUC-defined maximal tumour volumes of ≥2 cm^3. In Fig. 2b and Extended Data Figs. 2c,d and 3e, PDAC 1 is cell line 6419, PDAC 2 is cell line 50, PDAC 3 is cell line 6694, PDAC 4 is cell line 52, PDAC 5 is cell line 6499 and PDAC 6 is cell line 4662.

Anti-LTβR treatment. Mice were treated with 100 μg of anti-LTβR agonistic antibody (3C8, Invitrogen) or isotype control (Invitrogen) i.p. every 3 days as described[54].

DSS-colitis. 3% DSS (m/v) (MP Biomedicals) was dissolved in drinking water. Mice were iteratively exposed to DSS for 7 days, followed by 7 days of recovery[55], and euthanized for analyses at the indicated experimental timepoints. rIL-33 was initiated on day 0 of DSS treatment.

Acute ILC2 depletion with diphtheria toxin. *Nmur1*$^{icre\text{-}eGFP}$*Rosa*$^{LSL\text{-}DTR}$ mice or littermate control *Rosa*$^{LSL\text{-}DTR}$ mice were treated with twice daily i.p. injections of 100 ng DT (EMD Millipore) for 7 days beginning 2 days before tumour implantation, and every 2 days thereafter, as previously described[56].

Parabiosis. Female congenic CD45.1 and CD45.2 mice (aged 6 weeks) were surgically connected as previously described[32]. In brief, mice of similar body weight were co-housed 2 weeks before surgery and placed onto continuous prophylactic antibiotics (Sulfatrim diet, WF Fisher and Son) beginning the day before surgery. Lateral skin incisions from the elbow to knee were made on each mouse, and forelimbs and hindlimbs were sutured together. After surgery, mice were maintained on prophylactic sulfamethoxazole (Sulfatrim diet) for 2 weeks, followed by a normal diet thereafter. After confirming blood chimerism 4 weeks following parabiotic surgery, pancreatic and/or s.c. PDACs were implanted as described above. To ablate microbiota in parabiotic mice, after confirming blood chimerism, donor mice were treated with daily antibiotics (as described below) by oral gavage for 5 days before PDAC implantation, with subsequent antibiotic treatment maintained in the drinking water throughout the experimental duration. Parabionts were euthanized and organs were collected 14 days after tumour implantation.

Photoconversion. ILC2 migration was tracked using *CAG-KikGR*[57] mice that express Kikume Green-Red (KikGR) photoconvertible fluorescent protein. In brief, orthotopic PDACs were established, PDAC mice were treated daily with rIL-33 and, 6 days after tumour implantation, tissue was photoconverted[53]. To do so, a 1 cm incision was made into the abdominal wall, and the caecum and small intestine (gut) or peritoneum were photoconverted using a 405 nm violet laser for 10 min. PDACs were collected 2 days later to assess gut-derived photoconverted ILC2s by flow cytometry.

Microbiome ablation. Microbiome was ablated using an antibiotic cocktail of vancomycin (50 mg ml^{-1}; Sigma-Aldrich), neomycin (10 mg ml^{-1}; Sigma-Aldrich), metronidazole (100 mg ml^{-1}; Santa Cruz Biotech) and amphotericin (1 mg ml^{-1}; MP Biomedicals) administered daily by oral gavage for 5 days[36]. Orthotopic PDAC tumours were then implanted, and microbiome ablation was maintained with ampicillin (1 mg ml^{-1}; Sigma-Aldrich), vancomycin (0.5 mg ml^{-1}; Sigma-Aldrich), neomycin (0.5 mg ml^{-1}; Sigma-Aldrich), metronidazole (1 mg ml^{-1}; Santa Cruz Biotech) and amphotericin (0.5 μg ml^{-1}; MP Biomedicals) in the drinking water for the duration of the experiment.

Faecal microbiota transfer. To reconstitute microbiota in germ-free mice, fresh faecal samples were collected from WT C57BL/6 mice, resuspended in sterile PBS (6 faecal pellets per 1 ml of PBS), and 200 μl of the suspension was administered by oral gavage every other day for 2 weeks[36]. PDACs were then implanted and microbiome reconstitution was maintained with subsequent weekly faecal microbiota transfer.

Blood collection. Peripheral blood was collected from the submandibular vein of mice using a golden rod animal lancet (Medipoint) in plasma separation tubes with lithium heparin (BD Biosciences) and Microvette CB300Z (Sarstedt).

Microbiome analysis

DNA extraction and 16S library generation. Faecal samples were collected, DNA was extracted from single faecal pellets and deposited into a Qiagen PowerBead glass 0.1 mm tube (Qiagen) using the Promega Maxwell RSC PureFood GMO and Authentication Kit (Promega) according to the manufacturer's instructions. DNA was quantified using the Quant-iT dsDNA High Sensitivity Assay Kit with the Promega GloMax plate reader on a microplate (Fisher Scientific). 16S libraries were then generated as described previously (Earth Microbiome Project; https://earthmicrobiome.org/protocols-and-standards/16s/). Amplicon libraries were washed using Beckman Coulter AMPure XP magnetic beads, and the library quality and size were verified using the PerkinElmer LabChip GXII with the DNA 1K Reagent Kit (Perkin Elmer) according to the manufacturer's instructions. Libraries were normalized to 2 nM using the PerkinElmer Zephyr G3 NGS Workstation (Perkin Elmer) and pooled using identical volumes across normalized libraries into a 1.5 ml Eppendorf DNA tube.

Sequencing and data processing. Pooled libraries were sequenced (Illumina MiSeq) at a loading concentration of 7 pM with 15% PhiX, paired-end 250 (MiSeq Reagent Kit v2, 500-cycles). Demultiplexed raw reads were processed using the Nextflow[58], nf-core[59] ampliseq[60] pipeline (v.2.4.0), with the following parameters: -profile singularity --FW_primer GTGYCAGCMGCCGCGGTAA --RV_primer CCGYCAATT YMTTTRAGTTT --dada_ref_taxonomy silva --ignore_empty_input_files --ignore_failed_trimming --min_frequency 10 --retain_untrimmed --trunclenf 240 --trunclenr 160. Specifically, reads were trimmed with cutadapt[61], PhiX, and quality filtering, read pair merging and amplicon sequence variant resolution was performed with DADA2[62]. Subsequent taxonomic assignment was also performed with DADA2, using the Silva reference database[63] (v.138). Abundance tables were analysed using the QIIME2 software package. Tables were rarefied to 8,000 sequences for the Shannon diversity and principal component analyses.

Recombinant H-rIL-33 and H-e-rIL-33–Fc

H-rIL-33 and H-e-rIL-33–Fc proteins were produced by GenScript Biotech. In brief, target DNA sequences were codon-optimized, synthesized and subcloned into a cytomegalovirus promoter-driven expression vector following the human IL-2 signal peptide sequence. The proteins were expressed by transient transfection in HD Chinese hamster ovary cells and purified by affinity chromatography, followed by size-exclusion chromatography to obtain the desired purity. The purified protein was analysed by SDS–PAGE, western blotting and high-performance liquid chromatography analysis to determine the molecular mass and purity.

Recombinant IL-33, IL-25, H-rIL-33 and H-e-rIL-33–Fc treatment

After tumour implantation, mice were treated with i.p. injections of 500 ng carrier-free recombinant murine IL-33[16], IL-25 (R&D Systems) or H-rIL-33 (Proteos) daily for 7 days, and then every 2 days thereafter. For H-e-rIL-33–Fc, after tumour implantation, mice were treated every 2 days for 7 days, and then every 4 days thereafter at the indicated doses.

Human samples

All tissues were collected at MSK according to MSK Institutional Review Board (IRB) approved study protocols. Informed consent was obtained for all of the patients. The study was performed in strict compliance with all institutional ethical regulations. All tumour samples were surgically resected primary PDACs (for tumour transcriptomic profiling and serum IL-33 measurement; Supplementary Tables 1 and 3), or surgically resected human PDAC (immunohistochemistry/immunofluorescence, flow cytometry; Supplementary Tables 2 and 5). The human PDAC tissue microarrays[16], PDAC RNA-seq from ICGC[64] and human tumour sequencing from TCGA[65] have been previously described.

Tumour transcriptomic profiling

For the MSK cohort, primary PDACs from surgically resected patients with PDAC were randomly selected to undergo transcriptomic profiling as previously described[16]. In brief, total RNA from fresh-frozen OCT-embedded tumours was extracted using TRIzol RNA Isolation Reagents (Life Technologies), qualified on an Agilent BioAnalyzer, quantified by fluorometry (Ribogreen) and prepared for whole-transcriptome expression analysis using the WT Pico Reagent Kit (Affymetrix). RNA was then amplified using low-cycle PCR followed by linear amplification using T7 in vitro transcription technology. The cRNA was then converted to biotinylated sense-strand DNA hybridization targets, hybridized to GeneChip Human Transcriptome Array 2.0 (Affymetrix), scanned using the GeneChip Scanner 3000 and analysed using R (v.4.0.3).

For the TCGA cohort, RNA-seq datasets were obtained from https://gdc.cancer.gov/ under the identifiers of TCGA-PAAD[66] (TCGA PDAC cohort), TCGA-BRCA[67], TCGA-SKCM[68], TCGA-ACC, TCGA-BLCA, TCGA-KICH, TCGA-MESO, TCGA-PCPG, TCGA-PRAD, TCGA-TGCT or TCGA-UCS. For the ICGC cohort, RNA-seq data were obtained from previously published data[64]. For PDACs in all cohorts, patients with histologically diagnosed PDAC were included. All data were $\log_2$-transformed.

Cell isolation

Mouse and human PDACs and mouse intestines were mechanically dissociated and incubated in collagenase (collagenase II for mouse tumours, collagenase IV for human tumours, both 5 mg ml^{-1}; Worthington Biochemical, Thermo Fisher Scientific), DNase I (0.5 mg ml^{-1}; Roche Diagnostics) and Hank's balanced salt solution (Gibco, Thermo Fisher Scientific) for 30 min at 37 °C. Digestion was then quenched with FBS (Life Technologies). Digested tumours and DLNs were then mechanically disassociated and filtered through 100 mm and 40 mm nylon cell strainers (Falcon, Thermo Fisher Scientific) using PBS with 5% FBS (Life Technologies) and 4 mM EDTA (pH 8.0, Invitrogen). Spleens were mechanically dissociated and filtered through 70 mm and 40 mm nylon cell strainers (Falcon, Thermo Fisher Scientific) using PBS with 5% FBS and 2 mM EDTA, followed by red blood cell (RBC) lysis (RBC lysis buffer, Invitrogen Scientific). Peripheral blood was processed with RBC lysis and filtered through 40 mm nylon cell strainers. Mouse Fc receptors were blocked with FcεRIII/II-specific antibody (1 μg per 1×10^6 cells; 2.4G2, Bio XCell).

ILC2 and myeloid cell adoptive transfer

Donor orthotopic PDAC donor mice were treated with 500 ng carrier-free murine rIL-33 (R&D Systems) in sterile PBS daily for 10 days. For ILC2 transfer, live CD45$^+$lin$^-$CD90$^+$KLRG1$^+$ ILC2s from tumours were sort-purified to 98% purity at day 10 after implantation using the Aria Cell Sorter (BD Biosciences). Then, 5×10^4 ILC2s were immediately transferred to orthotopic PDAC-tumour-bearing *Il7r*$^{cre/+}$*Rora*$^{fl/fl}$ mice through i.p. injection 3 days after tumour implantation. For myeloid cell transfer, live CD45$^+$NK1.1$^-$CD11b$^+$LTβR$^+$ cells were sort-purified to 90% purity using the Aria Cell Sorter. For adoptive transfer, 5×10^5 CD11b$^+$LTβR$^+$ cells were mixed with tumour cell suspensions and injected into the tail of the pancreas using a 31-gauge needle. rIL-33 treatment (500 ng per mouse as described above) was administered in recipient mice on the day of ILC2 or myeloid cell transfer until the day of tissue collection. Tissues were collected at the indicated timepoints.

Flow cytometry

All of the samples were analysed on the FACS LSR Fortessa (BD Biosciences) system. Mouse ILC2s were defined as live CD45$^+$lin$^-$(CD3, CD5, NK1.1, CD11b, CD11c, CD19, FcεR1)CD90$^+$. Mouse KLRG1$^+$ ILC2s

were defined as live CD45$^+$lin$^-$(CD3, CD5, NK1.1, CD11b, CD11c, CD19, FcεR1)CD90$^+$KLRG1$^+$. All KLRG1$^+$ ILC2s as defined were confirmed to be GATA3$^+$ in our model (Extended Data Fig. 3a). Human ILC2s were defined as live CD45$^+$lin$^-$(CD3, CD5, CD56, CD11b, CD11c, CD14, CD16, CD19, TCRα/β, FcεR1)CD127$^+$CRTH2$^+$. Human KLRG1$^+$ ILC2s were defined as live CD45$^+$lin$^-$(CD3, CD5, CD56, CD11b, CD11c, CD14, CD16, CD19, TCRα/β, FcεR1)CD127$^+$CRTH2$^+$KLRG1$^+$. The following definitions were used for other immune cells: ILC1, live CD45$^+$lin$^-$TBET$^+$; ILC3, live CD45$^+$lin$^-$NK1.1$^-$RORγt$^+$; NK, live CD45$^+$CD3$^-$NK1.1$^+$; B cells, live CD45$^+$CD3$^-$NK1.1$^-$CD19$^+$; CD4$^+$ T cells, live CD45$^+$NK1.1$^-$CD3$^+$ CD8$^-$CD4$^+$; CD8$^+$ T cells, live CD45$^+$NK1.1$^-$CD3$^+$CD4$^-$CD8$^+$; Eosinophils, live CD45$^+$NK1.1$^-$CD3$^-$CD19$^-$CD11b$^+$SIGLECF$^+$; macrophages, live CD45$^+$ NK1.1$^-$CD3$^-$CD19$^-$CD11b$^+$F4/80$^+$; myeloid-derived suppressor cells (MDSCs), live CD45$^+$NK1.1$^-$CD3$^-$CD19$^-$CD11b$^+$SiglecF$^-$Gr-1$^+$; DCs, live CD45$^+$NK1.1$^-$CD3$^-$CD19$^-$Gr-1$^-$F4/80$^-$CD11c$^+$MHC-II$^+$.

Mouse cells were stained with the following antibodies according to the manufacturer's instructions: from BioLegend, CD11c (N418, BV510), CD19 (6D5, PE and BV785), CD25 (PC61, PerCP-Cy5.5), CD3 (145-2C11, BV711), CD4 (RM4-5, BV711 and BV786), CD45 (30-F11, Pacific Blue), CD45.1 (A20, BV711 and APC-Cy7), CD45.2 (104, Pacific Blue and APC-Cy7), CD8 (53-6.7, BV510), KLRG1 (2F1/KLRG1, BV510), LTBR (5G11, PE-Cy7), NK1.1 (PK136, BV605), SIGLECF (S17007L, APC), CD127 (A7R34, PE-Cy7) and Zombie Red Fixable Viability dye (423110); from BD Biosciences, CD11b (M1/70, Alexa Fluor 700, APC, and APC-Cy7), CD5 (53-7.3, APC), CD11c (HL3, APC), CD90.2 (53-2.1, BV786), GATA3 (L50-823, BV711 and PE), Gr-1 (RB6-8C5, BV605), NK1.1 (PK136, BV650 and APC), DRAQ7 (51-9011172), T-BET (O4-46, BV650), RORγt (Q31378, PE) and 4′,6-diamidino-2-phenylindole (DAPI); from Invitrogen Scientific, CD11c (N418, FITC), CD127 (A7R34, FITC), CD19 (eBio1D3, Alexa Fluor 700), CD3 (17A2, Alexa Fluor 700), CD8 (53-6.7, Alexa Fluor 700), F4/80 (BM8, PE-Cy5), FceR1 (MAR-1, APC), FOXP3 (FJK-16s, FITC), IL-33 (396118, PE), MHC class II (M5/114.15.2, Alexa Fluor 700), ST2 (RMST2-2, PE-Cy7) and TCRVβ (MR-9-4, Alexa Fluor 700).

To detect mouse LT, single-cell suspensions were incubated with recombinant mouse LTβR–Fc chimeric protein (1 μg ml^{-1}, R&D systems) in PBS with 5% FBS and 4 mM EDTA for 30 min in the dark at 4 °C, followed by incubation with a secondary antibody (goat anti-mouse IgG2a conjugated, Invitrogen) for 30 min in the dark at 4 °C, as previously described[69]. As positive controls, 3×10^6 bulk splenic T cells (isolated by negative selection using the mouse Pan T Cell Isolation Kit II, Miltenyi Biotech) from WT (positive control) or *Ltb*$^{-/-}$ (negative control) mice were stimulated in vitro with anti-CD3/anti-CD28 (1 μg ml^{-1}, BD Biosciences) in coated six-well plates with 10% RPM, 100 IU ml^{-1} penicillin and 100 μg ml^{-1} streptomycin for 4 h based on a previously described protocol[70] and examined for surface LT expression using identical staining methods as described above. To analyse mouse NMUR1 protein expression, single-cell suspension was first blocked with 2% normal mouse serum (Jackson ImmunoResearch) in FACS buffer (1% BSA, 2.5 mM EDTA, 25 mM HEPES, 0.05% sodium azide in PBS) followed by viability staining using LIVE/DEAD Fixable Aqua Dead Cell Stain dye (Thermo Fisher Scientific) in PBS. Cells were then incubated 30 min with anti-mouse NMUR1-biotinylated antibody (12-A03-A; previously described)[20] at 0.0173 mg ml^{-1} contained in the surface staining antibody mix. Then, after washing with FACS buffer, cells were counterstained with Streptavidin-BV650 conjugated fluorochrome at 1/250 dilution (BioLegend) for 15 min, followed by the intracellular staining and detection using the methods described above.

Human cells were stained with the following antibodies according to the manufacturer's instructions: from BD Biosciences, GATA3 (L50-823, PE); from BioLegend, CD11b (ICRF44, APC), CD45 (HI30, Pacific Blue), CD56 (HCD56, BV605), CRTH2 (BM16, PerCP/Cy5.5 and PE), FcεR1 (AER-37, APC), KLRG1 (2F1/KLRG1, BV510), TBET (4B10, BV711) and TCRα/β (IP26, APC); from Invitrogen Scientific, CD14 (61D3, APC), CD16 (CB16, APC), CD11c (3.9, APC), CD127 (RDR5, FITC), CD3 (OKT3, Alexa Fluor 700), CD5 (L17F12, APC) and CD19 (HIB19, AF700).

To detect human LT, single-cell suspensions were incubated with recombinant human LTβR–Fc chimeric protein (2 μg ml^{-1}, R&D systems, 629-LR) in PBS with 1% FBS and 0.5 mM EDTA (pH 8.0, Invitrogen) for 30 min in the dark at 4 °C followed by incubation with a secondary antibody (mouse anti-human IgG, Invitrogen) for 30 min in the dark at 4 °C. All of the samples for flow cytometry were from prospectively collected unselected patients (Supplementary Table 5).

H&E staining

Pancreatic tumours were cut into 2-mm-thick slices and fixed in 4% paraformaldehyde solution (Electron Microscopy Sciences), embedded in paraffin, stained with H&E, and scanned on the Panoramic Scanner (3DHistech) with the ×20/0.8 NA objective. The number of TLSs were determined in at least three sections using QuPath (v.0.2.3; https://qupath.github.io/). A compact aggregate of lymphocytes >5,000 μm^2 was considered as a TLS[71]. In DSS-colitis mice, lymphoid aggregates were counted in a section of a colon and normalized by the length of each colonic section.

Serum IL-33 detection

Human. Serum was collected and stored (−80 °C) until use. IL-33 levels were measured by multiplexed cytokine array (Human Cytokine/Chemokine 71-Plex Discovery Assay Array; Eve Technologies). Patient clinicopathological characteristics are shown in Supplementary Table 3.

Mouse. Serum was collected 48 h after the last rIL-33 dose and stored (−80 °C) until use. IL-33 levels were measured by multiplexed cytokine array (Mouse Cytokine Th17 12-Plex Discovery Assay, Eve Technologies).

Immunohistochemistry

Immunohistochemistry was performed on previously described human PDAC tissue microarrays[16]. In brief, paraffin-embedded tissue sections were deparaffinized with EZPrep buffer (Ventana Medical Systems). Antigen retrieval was performed with CC1 buffer (Ventana Medical Systems), followed by Background Buster solution (Innovex). Avidin-biotin blocking solution (Ventana Medical Systems) was then used to block tissue sections for 30 min. The sections were incubated with anti-human IL-33 antibody (AF3625, R&D System) for 4 h, followed by 60 min with biotinylated rabbit anti-goat IgG (Vector labs) at 1:200 dilution. IL-33 positivity was detected using the DAB detection kit (Ventana Medical Systems). Any cell demonstrating cytoplasmic or nuclear IL-33 positivity was designated to have positive staining. Nucleated cells in a TLS were determined and counted using the Analyse Particles function in ImageJ (v.2.3.0, NIH). IL-33$^+$ cells in a TLS were counted manually.

Immunofluorescence

Three-colour. Paraffin-embedded tissues were sliced into 7 μm sections. Multiplex immunofluorescence was performed using a Discovery XT processor (Ventana Medical Systems) as described previously[29]. To stain slides for B220, the sections were incubated with anti-B220 (RA3-6B2, BD Biosciences) for 6 h, followed by 60 min incubation with biotinylated horse anti-goat IgG (Vector Laboratories) at 1:200 dilution. Detection was performed with Streptavidin-HRP D (Ventana Medical Systems), followed by incubation with Tyramide Alexa Fluor 594 (Invitrogen) prepared according to the manufacturer's instructions with predetermined dilutions. The sections were then incubated with anti-CD3 (Dako) for 6 h, followed by 60 min incubation with biotinylated goat anti-rabbit IgG (Vector Laboratories) at 1:200 dilution. Detection was performed with Streptavidin-HRP D (Ventana Medical Systems), followed by incubation with Tyramide Alexa 488 (Invitrogen) prepared according to the manufacturer's instructions with predetermined dilutions. Finally, the sections were incubated with anti-LYVE-1 (R&D systems) for 6 h, followed by 60 min incubation with biotinylated goat anti-rabbit IgG (Vector Laboratories) at 1:200 dilution. Detection was performed with Streptavidin-HRP D (Ventana Medical Systems),

followed by incubation with Tyramide Alexa 647 (Invitrogen) prepared according to the manufacturer's instructions with predetermined dilutions. After staining, the slides were counterstained with DAPI (Sigma-Aldrich) for 10 min and cover-slipped with Mowiol.

Five-colour in mice. Paraffin-embedded tissues were sliced into 7 µm sections. Multiplex immunofluorescence was performed using a Discovery XT processor (Ventana Medical Systems) as described[29]. The sequential antibody staining was conducted as follows: 6 h incubation with anti-MECA-79 (BD Pharmingen) followed by 60 min incubation with secondary antibody (Al488); 6 h incubation with anti-BCL6 (Abcam) followed by 60 min incubation with secondary antibody (CF594); 6 h incubation with anti-CD11c (Cell Signaling) followed by secondary antibody (Al647); 6 h incubation with anti-CD3 (Dako) followed by secondary antibody (CF543); and 6 h incubation with anti-B220 (BD BioScience) followed by secondary antibody (CF430). For TLS quantification, the number of TLSs was determined in at least three sections using CaseViewer (3DHISTECH). Mouse TLSs were determined as a compact aggregate of T and B lymphocytes and high endothelial venules. TLS maturation states[72–74] were defined as follows: lymphoid aggregates, $CD3^+B220^+CD11c^-MECA\text{-}79^-BCL6^-$; primary follicles, $CD3^+B220^+CD11c^+MECA\text{-}79^+BCL6^-$.

Five-colour in humans. Automated multiplex immunofluorescence was conducted using the Leica Bond BX staining system. Paraffin-embedded tissues were sectioned at a thickness of 5 µm and baked at 58 °C for 1 h. The slides were loaded in Leica Bond and staining was performed as follows. The samples were pretreated with EDTA-based epitope retrieval ER2 solution (Leica, AR9640) for 20 min at 100 °C. The 4-plex antibody staining and detection were conducted sequentially. The primary antibodies against IL-33 (1.25 µg ml^{-1}, R&D Systems), MECA-79 (1.25 µg ml^{-1}, BD Pharmingen), CD21 (5 µg ml^{-1}, Leica Biosystems), CD45 (0.625 µg ml^{-1}, Abcam) and CD3 (1:10, Roche Diagnostics) were used.

For rabbit antibodies, Leica Bond Polymer anti-rabbit HRP was used; for goat, rat and mouse antibodies, rabbit anti-goat (Jackson ImmunoResearch), rabbit anti-rat (Vector Laboratories) and rabbit anti-mouse (Abcam) secondary antibodies were used before applying the Leica Bond Polymer anti-rabbit HRP. Next, Alexa Fluor tyramide signal amplification reagents (Life Technologies) or CF dye tyramide conjugates (Biotium) were used for detection. After each round of immunofluorescence staining, epitope retrieval was performed to denature primary and secondary antibodies before applying another primary antibody. The slides were then washed in PBS and incubated in 5 µg ml^{-1} DAPI (Sigma-Aldrich) in PBS for 5 min, rinsed with PBS and mounted in Mowiol 4–88 (Calbiochem). The slides were kept overnight at −20 °C before imaging. CD45 and IL-33 positivity was determined by CaseViewer (3DHISTECH). $IL\text{-}33^+$ and $IL\text{-}33^+CD45^+$ cells were quantified on ImageJ (National Institute of Health), and cells per area estimated by calculating surface area based on presence of $DAPI^+$ cells. Human TLSs were determined as compact aggregate structures of T cells ($CD45^+CD3^+$)[7,75], B cells ($CD45^+CD21^+$)[7,75] and high endothelial venules ($MECA\text{-}79^+$)[6].

B cell receptor sequencing

Mouse B cell receptor sequencing was done by Adaptive Biotechnology. In brief, ten 5 µm curls of FFPE blocks for each sample were preserved at −80 °C. DNA was extracted, and immunosequencing of the CDR3 regions of mouse B cell receptor chains was performed on genomic DNA from FFPE-fixed samples using the immunoSEQ Assay (Adaptive Biotechnologies[76]). All of the samples were amplified in a bias-controlled multiplex PCR, followed by high-throughput sequencing, identification and quantification of absolute abundances of unique CDR3 regions. The resulting sequencing data were processed and analysed on the immunoSEQ Analyser web-based relational database.

Somatic hypermutation

All rearrangements were exported to FASTA files using the Fasta Conversion tool in the Immunoseq Analyzer web-based platform and input to the nf-core/airrflow pipeline for analysis using the Immcantation toolset[77]. Each rearrangement was annotated with its germline V(D)J gene allele using IgBlast with the Mus musculus IMGT germline reference v.2022.10.04 (http://www.imgt.org/IMGT_GENE-DB). Rearrangements with productive heavy-chain sequences were retained for analysis of B cell clonal relationships, and clones were defined by VDJ-aware spectral clustering using the R package SCOPer[78]. Mutation frequencies were computed using the observed mutations function in the R package Shazam[79].

Digital droplet PCR

For purified cells, frozen cells were lysed in 1 ml of TRIzol Reagent (Thermo Fisher Scientific), and phase separation was induced with 200 µl of chloroform. RNA was extracted from 350 µl of the aqueous phase using the miRNeasy Micro Kit (Qiagen) on the QIAcube Connect (Qiagen) according to the manufacturer's protocol. The samples were eluted in 30 µl of RNase-free water.

For whole intestine, frozen tissues were homogenized in in TRIzol (Thermo Fisher Scientific), and phase separation was induced with 200 µl of chloroform. RNA was extracted from the aqueous using the MagMAX mirVana Total RNA Isolation Kit (Thermo Fisher Scientific) on the KingFisher Flex Magnetic Particle Processor (Thermo Fisher Scientific) according to the manufacturer's protocol with 350 µl input. Samples were eluted in 35 µl of elution buffer.

PCR expression probes were designed (Bio-Rad) for the following genes: mouse *Il33* (dMmuCPE5096722), *Ltbr* (dMmuCPE5113608), *Ccl19* (dMmuCPE5092188), *Cxcl9* (dMmuCPE5122450) and *Cxcl13* (dMmuCPE5110356). Droplet generation was performed on the QX200 ddPCR system (Bio-Rad) using cDNA generated from 0.8–2 ng total RNA with the One-Step RT-ddPCR Advanced Kit for Probes (Bio-Rad) according to the manufacturer's protocol with reverse transcription at 42 °C and annealing/extension at 60 °C. Each sample was evaluated in technical duplicates. Plates were read and analysed (QuantaSoft) to assess the number of droplets positive for genes of interest. The number of droplets was normalized to the input amount of total RNA.

scRNA-seq

Library preparation, sequencing and post-processing for single-cell immune profiling have been previously described[16]. In brief, $ST2^+$ ILC2s were purified from tumours and DLNs from PDAC mice treated with rIL-33 for 10 days, and $CD45^+CD11b^+LTBR^+$ and $CD45^+CD11b^+LTBR^-$ cells were purified from tumours of PDAC mice treated with rIL-33 for 14 days. scRNA-seq libraries were prepared according to the manufacturer's recommendations (Chromium Single Cell V(D)J User Guide PN-1000006, 10x Genomics). Cell suspensions (85–90% viable) at a concentration of 90–200 cells per µl were loaded onto the 10x Genomics Chromium platform to generate Gel Beads in Emulsion (GEMs), targeting about 2,000 single cells per sample. After GEM generation, the samples were incubated at 53 °C for 45 min in the C1000 Touch Thermal cycler with a 96-Deep Well Reaction Module (BioRad) to generate poly(A) cDNA barcoded at the 5′ end by the addition of a template switch oligo linked to a cell barcode and unique molecular identifiers (UMIs). After breaking the GEMs, the single-stranded cDNA was cleansed with DynaBeads MyOne Silane Beads (Thermo Fisher Scientific). The cDNA was then amplified (98 °C for 45 s; then 16 cycles of 98 °C for 20 s, 67 °C for 30 s, 72 °C for 1 h), after which the cDNA quality was assessed using the Agilent Bioanalyzer 2100, obtaining a product of about 1,200 bp. cDNA (50 ng) was enzymatically fragmented, end repaired, A-tailed, subjected to a double-sided size selection with SPRI select beads (Beckman Coulter) and ligated to adaptors provided in the kit. Within each library, a unique sample kit was then introduced through 14 cycles of PCR amplification using the

indexes provided in the kit (98 °C for 45 s; 14 cycles of 98 °C for 20 s, 54 °C for 30 s, 72 °C for 20 s; 72 °C for 1 min; then held at 4 °C). A second double-sided selection was then performed on the indexed libraries, after which the libraries were quantified using Qubit fluorometric quantification (Thermo Fisher Scientific). The Agilent Bioanalyzer 2100 was used to assess the quality (average library size 450 bp), after which cDNA was amplified with 18 cycles, and a unique sample index was added to each library in 16 cycles. Diluted libraries were then clustered using the NovaSeq 600 system on a paired-end read flow cell, sequenced for 28 cycles on R1 (10x barcode and the UMIs), followed by 8 cycles of 17 index (sample index), and 89 bases on R2 transcript, obtaining approximately 100 million clusters per samples. Primary processing of sequencing images was done using Illumina's Real Time Analysis software (RTA). 10x Genomics Cell Ranger Single Cell Software suite v.3.0.2 (https://support.10xgenomics.com/single-cell-gene-expression/software/pipelines/latest/what-is-cellranger) was used to demultiplex samples, align to the mouse genomic reference mm10, filter, count UMIs, single-cell 5′ end genes and control quality according to the manufacturer's parameters. Processed data were subsequently analysed in R (v.4.0.3).

To estimate a TLS chemokine signature[7] in myeloid cells, a signature score was computed for the 12 chemokines[7] using the GSVA method[80] in R (v.4.0.3). In brief, to achieve quality control, low-quality cells were filtered out based on the median absolute deviation of unique feature counts and mitochondrial counts[81], followed by normalization using a global-scaling method. Assay data were then extracted and applied as the expression set, with the 12 chemokines (CCL2, CCL3, CCL4, CCL5, CCL8, CCL18, CCL19, CCL21A, CCL21B, CXCL9, CXCL10, CXCL11 and CXCL13) provided as a reference gene set using the GSVA function. The ensuing consensus expression was projected onto target cell populations using UMAP and violin plot visualizations.

TLS and ILC2 transcriptional signatures

Known TLS gene signatures were extracted from each transcriptomic dataset (see the 'Tumour transcriptomic profiling' section). In brief, the signatures included the genes *CD79B*, *EIF1AY*, *PTGDS*, *CCR6*, *SKAP1*, *CETP* and *CD1D* in ref. 4; *CCL2*, *CCL3*, *CCL4*, *CCL5*, *CCL8*, *CCL18*, *CCL19*, *CCL21*, *CXCL9*, *CXCL10*, *CXCL11* and *CXCL13* in ref. 7; and *CXCL13*, *CD200*, *FBLN7*, *ICOS*, *SGPP2*, *SH2D1A*, *TIGIT* and *PDCD1* in ref. 8. The signature score was calculated as the mean gene expression. Pearson's correlation tests were performed using the rcorr function of the Hmisc package (v.4.5) in R (v.4.0.3).

To establish a human intratumoural ILC2 transcriptional signature (ILC2 score), we first identified candidate differentially expressed genes in rIL-33-activated KLRG1$^+$ ILC2s in tumours and DLNs of PDAC mice, based on purified single-cell transcriptomes (from scRNA-seq above) using the Seurat package on R. After unsupervised clustering, we computed differentially expressed genes for each cluster in the dataset shown in Fig. 3a using Wilcoxon rank-sum test with adjustment for multiple comparisons. As a result, we identified 341 genes significantly and specifically upregulated in KLRG1$^+$ ILC2s (cluster 0).

We next identified human orthologues of the 341 genes upregulated in mouse KLRG1$^+$ ILC2s using the Ensembl Biomart database[82], and identified genes with unique human orthologues. We next downloaded the raw read counts for the primary pancreatic cancers (PAAD) from the RNA-seq TCGA dataset using TCGAbiolinks R package[83–85]. We removed non-coding genes from the read count matrix, as well as genes with <1 read per million in at least 5% of the samples in the dataset. We then restricted the ILC2 gene list to the genes expressed (as defined above) in the TCGA PAAD dataset, ordered them by the statistical significance in the mouse differential expression analysis and selected the top 20 genes to serve as the human ILC2 score (*LAPTM5*, *IL7R*, *TSPAN13*, *LY6E*, *S100A10*, *S100A6*, *HSPA8*, *SELPLG*, *ITM2B*, *B2M*, *CORO1A*, *PFN1*, *MYL12B*, *CNN2*, *RAC2*, *TSPO*, *TMSB4Y*, *PTPN18*, *CD52* and *RPL37A*).

To evaluate the relationship between this ILC2 score and TLS signatures[4,7,8], we computed the log-transformed normalized gene expression in the TCGA-PAAD dataset described above using the TMM method[86] from edgeR package. Consensus expression of the three existing TLS signatures and the new ILC2 score was computed using the GSVA method[80]. We ran *t*-tests for Pearson correlations between the consensus expression of the ILC2 score and each of the three existing TLS signatures and applied the Bonferroni correction for multiple testing.

Confocal microscopy

To visualize LT expression on KLRG1$^+$ ILC2s, PDAC mice were treated with rIL-33 for 2 weeks, intratumoural KLRG1$^+$ ILC2s were sort purified and surface LT expression was detected with recombinant mouse LTβR–Fc chimeric protein (1 μg ml^{-1}, R&D systems) as described above (see the 'Flow cytometry' section). Sort-purified KLRG1$^+$ ILC2s and MACS-purified CD3/28-stimulated T cells were incubated with recombinant mouse LTβR–Fc chimeric protein (1 μg ml^{-1}, R&D systems) in 5% FBS at 4 °C for 30 min. Cells were then stained with PE-conjugated anti-mouse IgG2a antibody (Invitrogen) at 4 °C for 30 min. Cells were then settled on 0.01% polylysine-coated coverslips for 30 min at room temperature, fixed on coverslips with 4% PFA and permeabilized with 0.1% Triton X-100 for 20 min at room temperature. The coverslips with fixed cells were mounted with Molecular Probes SlowFade Diamond Antifade Mountant with DAPI (Thermo Fisher Scientific).

To visualize LT–PE and nuclear DAPI, the images were taken on a point laser-scanning confocal system (SP5, Leica) with a ×63 oil-immersion using objective 2 (×2 visual magnification). Images with binomial signals were visualized using ImageJ.

In vitro studies

ST2 reporter assay. A total of 5×10^4 HEK-Blue IL-33 cells (Invivogen) was seeded onto 96-well plates with DMEM, 10% FBS, penicillin (100 IU ml^{-1}) and streptomycin (100 μg ml^{-1}). Cells were incubated for 24 h at 37 °C in 5% CO_2 with H-rIL-33 (Proteos), H-e-rIL-33 or H-e-rIL-33–Fc at the designated concentrations. After incubation, 20 μl of supernatant was added to 180 μl of QUANTI-Blue solution (Invivogen) per well in a flat-bottom 96-well plate. The plate was incubated for 2 h at 37 °C in 5% CO_2 followed by 630-nm-wavelength absorbance detection on the Cytation 3 reader (BioTek).

Statistics

Comparisons between two groups were performed using unpaired Mann–Whitney *U*-test with the Benjamini–Krieger–Yekutieli false-discovery approach for multiple-timepoint comparisons (two-tailed). Comparisons among multiple groups were performed using one-way ANOVA followed by Kruskal–Wallis multiple-comparison post-test. Comparisons among multiple groups across multiple timepoints were performed using two-way ANOVA followed by Šidák's multiple-comparison post-test. EC_{50} curves were compared using an extra sum of squares *F* test. Correlations between two variables were calculated using linear regression. All alpha levels were 0.05; $P < 0.05$ was considered to be a significant difference. Statistical analyses were performed using R (v.4.0.3, scRNA-seq) and Prism v.9.2.0 (GraphPad Software, all else).

Material availability

All material is available from the corresponding author on reasonable request.

Reporting summary

Further information on research design is available in the Nature Portfolio Reporting Summary linked to this article.

Data availability

Source data are provided for all experiments. RNA-seq data from the TCGA and ICGC are publicly available[64,65]. All other bulk RNA expression

data are available under Gene Expression Omnibus (GEO) accession number GSE184585. scRNA-seq data of ILC2s have been previously reported[16] and are available under GEO accession number GSE136720. scRNA-seq data of myeloid cells are available under GEO accession number GSE225990. 16S rRNA gene sequencing data are available under BioProject ID number PRJNA944673. Source data are provided with this paper.

51. Tumanov, A. et al. Distinct role of surface lymphotoxin expressed by B cells in the organization of secondary lymphoid tissues. *Immunity* **17**, 239–250 (2002).
52. Fütterer, A., Mink, K., Luz, A., Kosco-Vilbois, M. H. & Pfeffer, K. The lymphotoxin beta receptor controls organogenesis and affinity maturation in peripheral lymphoid tissues. *Immunity* **9**, 59–70 (1998).
53. Nowotschin, S. & Hadjantonakis, A.-K. Use of KikGR a photoconvertible green-to-red fluorescent protein for cell labeling and lineage analysis in ES cells and mouse embryos. *BMC Dev. Biol.* **9**, 49 (2009).
54. Haybaeck, J. et al. A lymphotoxin-driven pathway to hepatocellular carcinoma. *Cancer Cell* **16**, 295–308 (2009).
55. Wirtz, S. et al. Chemically induced mouse models of acute and chronic intestinal inflammation. *Nat. Protoc.* **12**, 1295–1309 (2017).
56. Arifuzzaman, M. et al. Dietary fiber is a critical determinant of pathologic ILC2 responses and intestinal inflammation. *J. Exp. Med.* **221**, e20232148 (2024).
57. Zegarra-Ruiz, D. F. et al. Thymic development of gut-microbiota-specific T cells. *Nature* **594**, 413–417 (2021).
58. Tommaso, P. D. et al. Nextflow enables reproducible computational workflows. *Nat. Biotechnol.* **35**, 316–319 (2017).
59. Ewels, P. A. et al. The nf-core framework for community-curated bioinformatics pipelines. *Nat. Biotechnol.* **38**, 276–278 (2020).
60. Straub, D. et al. Interpretations of environmental microbial community studies are biased by the selected 16S rRNA (gene) amplicon sequencing pipeline. *Front. Microbiol.* **11**, 550420 (2020).
61. Martin, M. Cutadapt removes adapter sequences from high-throughput sequencing reads. *EMBnet J.* https://doi.org/10.14806/ej.17.1.200 (2011).
62. Callahan, B. J. et al. DADA2: high-resolution sample inference from Illumina amplicon data. *Nat. Methods* **13**, 581–583 (2016).
63. Quast, C. et al. The SILVA ribosomal RNA gene database project: improved data processing and web-based tools. *Nucleic Acids Res.* **41**, D590–D596 (2013).
64. Bailey, P. et al. Genomic analyses identify molecular subtypes of pancreatic cancer. *Nature* **531**, 47–52 (2016).
65. Liu, J. et al. An integrated TCGA pan-cancer clinical data resource to drive high-quality survival outcome analytics. *Cell* **173**, 400–416 (2018).
66. Raphael, B. J. et al. Integrated genomic characterization of pancreatic ductal adenocarcinoma. *Cancer Cell* **32**, 185–203.e13 (2017).
67. Berger, A. C. et al. A comprehensive pan-cancer molecular study of gynecologic and breast cancers. *Cancer Cell* **33**, 690–705 (2018).
68. Network, T. C. G. A. et al. Genomic classification of cutaneous melanoma. *Cell* **161**, 1681–1696 (2015).
69. Bando, J. K., Liang, H.-E. & Locksley, R. M. Identification and distribution of developing innate lymphoid cells in the fetal mouse intestine. *Nat. Immunol.* **16**, 153–160 (2014).
70. Chiang, E. Y. et al. Targeted depletion of lymphotoxin-α–expressing TH1 and TH17 cells inhibits autoimmune disease. *Nat. Med.* **15**, 766–773 (2009).
71. Rodriguez, A. B. et al. Immune mechanisms orchestrate tertiary lymphoid structures in tumors via cancer-associated fibroblasts. *Cell Rep.* **36**, 109422 (2021).
72. Silina, K. et al. Germinal centers determine the prognostic relevance of tertiary lymphoid structures and are impaired by corticosteroids in lung squamous cell carcinoma. *Cancer Res.* **78**, 1308–1320 (2017).
73. Posch, F. et al. Maturation of tertiary lymphoid structures and recurrence of stage II and III colorectal cancer. *Oncoimmunology* **7**, e1378844 (2017).
74. Calderaro, J. et al. Intra-tumoral tertiary lymphoid structures are associated with a low risk of early recurrence of hepatocellular carcinoma. *J. Hepatol.* **70**, 58–65 (2019).
75. Vanhersecke, L. et al. Mature tertiary lymphoid structures predict immune checkpoint inhibitor efficacy in solid tumors independently of PD-L1 expression. *Nat. Cancer* **2**, 794–802 (2021).
76. Carlson, C. S. et al. Using synthetic templates to design an unbiased multiplex PCR assay. *Nat. Commun.* **4**, 2680 (2013).
77. Gabernet, G. et al. nf-core/airrflow: an adaptive immune receptor repertoire analysis workflow employing the Immcantation framework. *PLoS Comput. Biol.* **20**, e1012265 (2024).
78. Nouri, N. & Kleinstein, S. H. Somatic hypermutation analysis for improved identification of B cell clonal families from next-generation sequencing data. *PLoS Comput. Biol.* **16**, e1007977 (2020).
79. Gupta, N. T. et al. Change-O: a toolkit for analyzing large-scale B cell immunoglobulin repertoire sequencing data. *Bioinformatics* **31**, 3356–3358 (2015).
80. Hänzelmann, S., Castelo, R. & Guinney, J. GSVA: gene set variation analysis for microarray and RNA-seq data. *BMC Bioinform.* **14**, 7 (2013).
81. McCarthy, D. J., Campbell, K. R., Lun, A. T. L. & Wills, Q. F. Scater: pre-processing, quality control, normalization and visualization of single-cell RNA-seq data in R. *Bioinformatics* **33**, btw777 (2017).
82. Cunningham, F. et al. Ensembl 2022. *Nucleic Acids Res.* **50**, D988–D995 (2021).
83. Colaprico, A. et al. TCGAbiolinks: an R/Bioconductor package for integrative analysis of TCGA data. *Nucleic Acids Res.* **44**, e71 (2016).
84. Silva, T. C. et al. TCGA Workflow: analyze cancer genomics and epigenomics data using Bioconductor packages. *F1000Res.* **5**, 1542 (2016).
85. Mounir, M. et al. New functionalities in the TCGAbiolinks package for the study and integration of cancer data from GDC and GTEx. *PLoS Comput. Biol.* **15**, e1006701 (2019).
86. Robinson, M. D. & Oshlack, A. A scaling normalization method for differential expression analysis of RNA-seq data. *Genome Biol.* **11**, R25 (2010).

Acknowledgements This work was supported by NIH R01 CA262516 (V.P.B.), NIH P50 CA257881 (V.P.B.), a Damon Runyon Clinical Investigator Continuation Award (V.P.B.), a Pershing Square Sohn Prize for Young Investigators (V.P.B.), the Ben and Rose Cole PRIA Foundation Scholar Award (V.P.B.), the Sarah Min and Matthew Pincus Pancreatic Cancer Immunotherapy Award (V.P.B.), the Ludwig Institute for Cancer Research (T.M.), Swim Across America (T.M.) and the Parker Institute (T.M.). D.A. receives support from CURE for IBD, the Jill Roberts Institute for Research in IBD, Kenneth Rainin Foundation, the Sanders Family Foundation, Rosanne H. Silbermann Foundation, Linda and Glenn Greenberg, the Allen Discovery Center Program, a Paul G. Allen Frontiers Group advised program of the Paul G. Allen Family Foundation and the National Institutes of Health (DK126871, AI151599, AI095466, AI095608, AR070116, AI172027, DK132244). H.Y. is supported by a Crohn's and Colitis Foundation Research Fellowship Award (937437) and National Institutes of Health K99AI180354. Services of the Integrated Genomics Core were funded by the NCI Cancer Center Support Grant (P30 CA08748), Cycle for Survival, and the Marie-Josée and Henry R. Kravis Center for Molecular Oncology. Services for the 16S rRNA-seq were performed at the Microbiome Core Laboratory at Weill Cornell Medicine. We acknowledge the support of the staff at the Tri-Institutional Therapeutics Discovery Institute (TDI), a 501(c)(3) organization. The TDI receives financial support from Takeda Pharmaceutical Company, TDI's parent institutes (Memorial Sloan Kettering Cancer Center, The Rockefeller University and Weill Cornell Medicine) and a contribution from L. Sanders and other philanthropic sources.

Author contributions V.P.B. conceived the study. M.A., A.Z. and V.P.B. designed all of the experiments. M.A. and A.Z. performed and interpreted all of the experiments with assistance from L.A.R., P.G., A.K.C., G.P., R.Y., T.W., H.Y., D.A. and Z.O. M.A., A.Z., A.G.K., I.C.L., O.V., M.B., T.M. and V.P.B. designed H-e-rIL-33–Fc. O.V., E.K.N., I.C.L., M.B. and A.G.K. coordinated and synthesized H-e-rIL-33–Fc. A.S. and B.G. derived the ILC2 transcriptional signature. A.Z., S.M. and B.G. performed the microbiome analyses. M.G. provided statistical oversight, and R.G. oversaw flow cytometry data analysis. A.V.T. provided mice and technical guidance. E.P. provided editorial oversight. M.A., A.Z., H.Y., S.L.Z., G.P., A.K.C., R.Y., P.G., Z.M.S., A.O., L.A.R., C.C., T.W., A.S., S.M., A.S.D., C.R., E.M.B., M.M., K.S., Z.O., J.A.M., J.N.Z., M.G., R.G., A.V.T., A.G.K., O.V., E.K.N., I.C.L., M.B., E.P., B.G., D.A., T.M. and V.P.B. analysed and interpreted the data. M.A., A.Z. and V.P.B. wrote the manuscript with input from all of the authors.

Competing interests O.V., E.K.N., I.C.L., M.B. and A.G.K. (employees of the Tri-Institutional Therapeutics Discovery Institute) may benefit from the further development and licensure of molecules described here. L.A.R. is listed as an inventor of a patent related to oncolytic viral therapy. V.P.B. reports honoraria from Genentech, and Abbvie, research support from Bristol Myers Squibb and Genentech, has consulted for Merck and is listed as an inventor on a patent application related to the use of IL-33 and enhanced IL-33 for cancer immunotherapy. T.M. reports that he is a consultant for Daiichi Sankyo, Leap Therapeutics, Immunos Therapeutics and Pfizer, and co-founder of Imvaq Therapeutics. T.M. has equity in Imvaq therapeutics. T.M. has received research funding from Surface Oncology, Kyn Therapeutics, Infinity Pharmaceuticals, Peregrine Pharmaceuticals, Adaptive Biotechnologies, Leap Therapeutics and Aprea Therapeutics, and currently receives research funding from Bristol-Myers Squibb, Enterome SA and Realta Life Sciences. T.M. is listed as an inventor on patent applications related to work on oncolytic viral therapy, alphavirus-based vaccines, neo-antigen modelling, CD40, GITR, OX40, PD-1 and CTLA-4. D.A. has contributed to scientific advisory boards at Pfizer, Takeda, FARE and the KRF. The other authors declare no competing interests.

Additional information

Supplementary information The online version contains supplementary material available at https://doi.org/10.1038/s41586-024-08426-5.

Correspondence and requests for materials should be addressed to Vinod P. Balachandran.

Peer review information *Nature* thanks Shigeo Koyasu and the other, anonymous, reviewer(s) for their contribution to the peer review of this work.

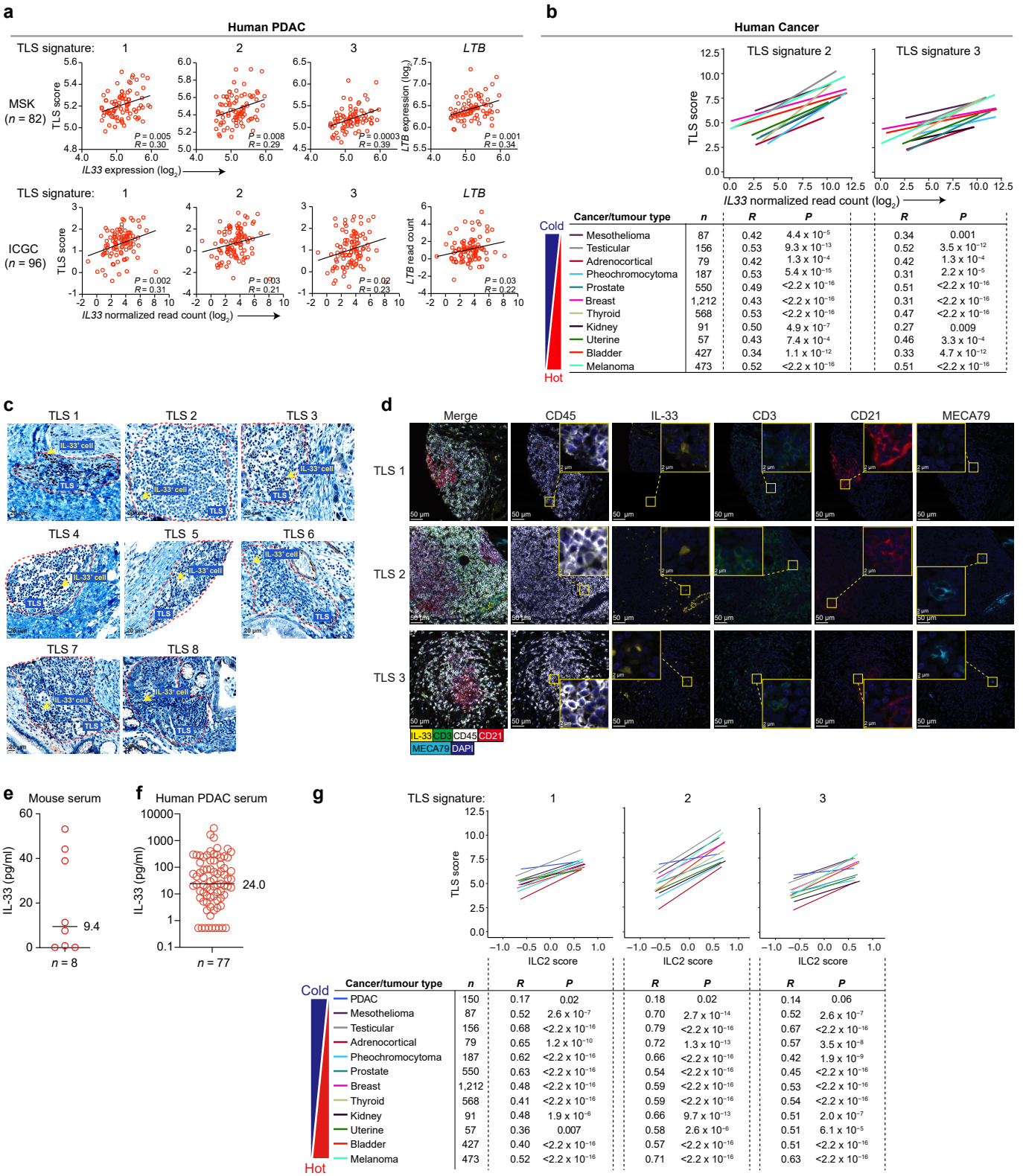

Extended Data Fig. 1 | Intratumoural *IL33* expression in human tumours. **a, b**, Correlation of intratumoural *IL33* mRNA expression to TLS transcriptional signatures (TLS signature: 1[4], 2[7], 3[8]), and *LTB* mRNA expression in human PDAC cohorts (**top**, Memorial Sloan Kettering Cancer Center (MSK) cohort; **bottom**, International Cancer Genome Consortium (ICGC) cohort) and human tumours from the Cancer Genome Atlas (**b**). **c**, IL-33 immunohistochemistry in human PDACs with TLSs. Dotted red lines = putative TLS. **d**, Immunofluorescence images of TLSs in human PDACs. **e, f**, Serum IL-33 in rIL-33-treated PDAC mice (**e**) and in human PDAC patients (**f**). **g**, Correlation of IL-33-activated human ILC2 transcriptional signature to TLS signatures (TLS signatures: 1[4], 2[7], 3[8]) in human tumours from the Cancer Genome Atlas. *n* = number of tumours (**a**, **b**, **g**), mice (**e**) or patients (**f**). Data collected at 4 weeks (**e**) after tumour implantation, pooled from 2 independent experiments with $n \geq 3$ mice per group with consistent results. *P* values by two-sided Pearson's correlation (**a**, **b**, **g**).

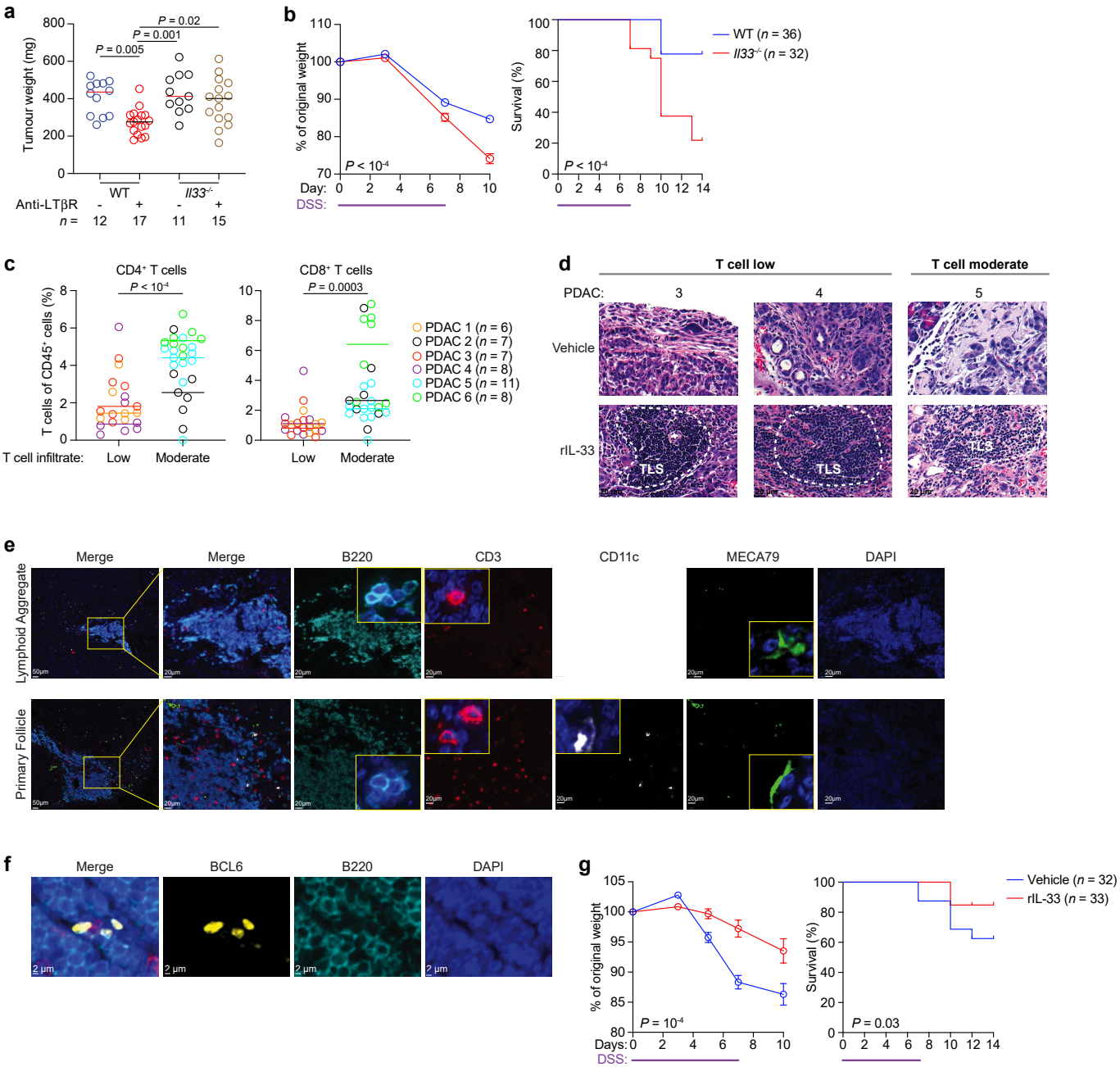

Extended Data Fig. 2 | Disease and immune activity with IL-33 modulation in PDAC and DSS-colitis. a, Tumour weight in anti-LTβR-treated WT and *Il33*$^{-/-}$ PDAC mice. **b**, Weight loss and survival in WT and *Il33*$^{-/-}$ DSS-colitis mice. **c**, Frequency of CD4^{+} and CD8^{+} T cells in PDAC mouse models with low and moderate T cell infiltration. **d**, H&E of TLSs in T cell low and T cell moderate tumours. Dotted white lines = putative TLS. **e, f**, Immunofluorescence images of intratumoural lymphoid aggregates and primary follicles (**e**) and TLSs with BCL6^{+} B cells (**f**) in rIL-33-treated PDAC mice. **g**, Weight loss and survival in vehicle-treated and rIL-33-treated DSS-colitis mice. Data collected 2 (**a**), 3 (**c, d** PDAC 3, 4) and 3–5 (**c, d** PDAC 1, 2, 5, 6, **e, f**) weeks after tumour implantation, pooled from ≥2 independent experiments with $n \geq 3$ mice per group with consistent results. *n* = individual tumours from individual mice or individual mice analysed separately. Horizontal bars = median. *P* values by one-way ANOVA with Tukey's multiple comparison test (**a**), two-tailed Mann-Whitney *U*-test (**c**), two-way ANOVA with Sidak's multiple comparison test (**b, g**, weight loss), and log rank test (**b, g**, survival).

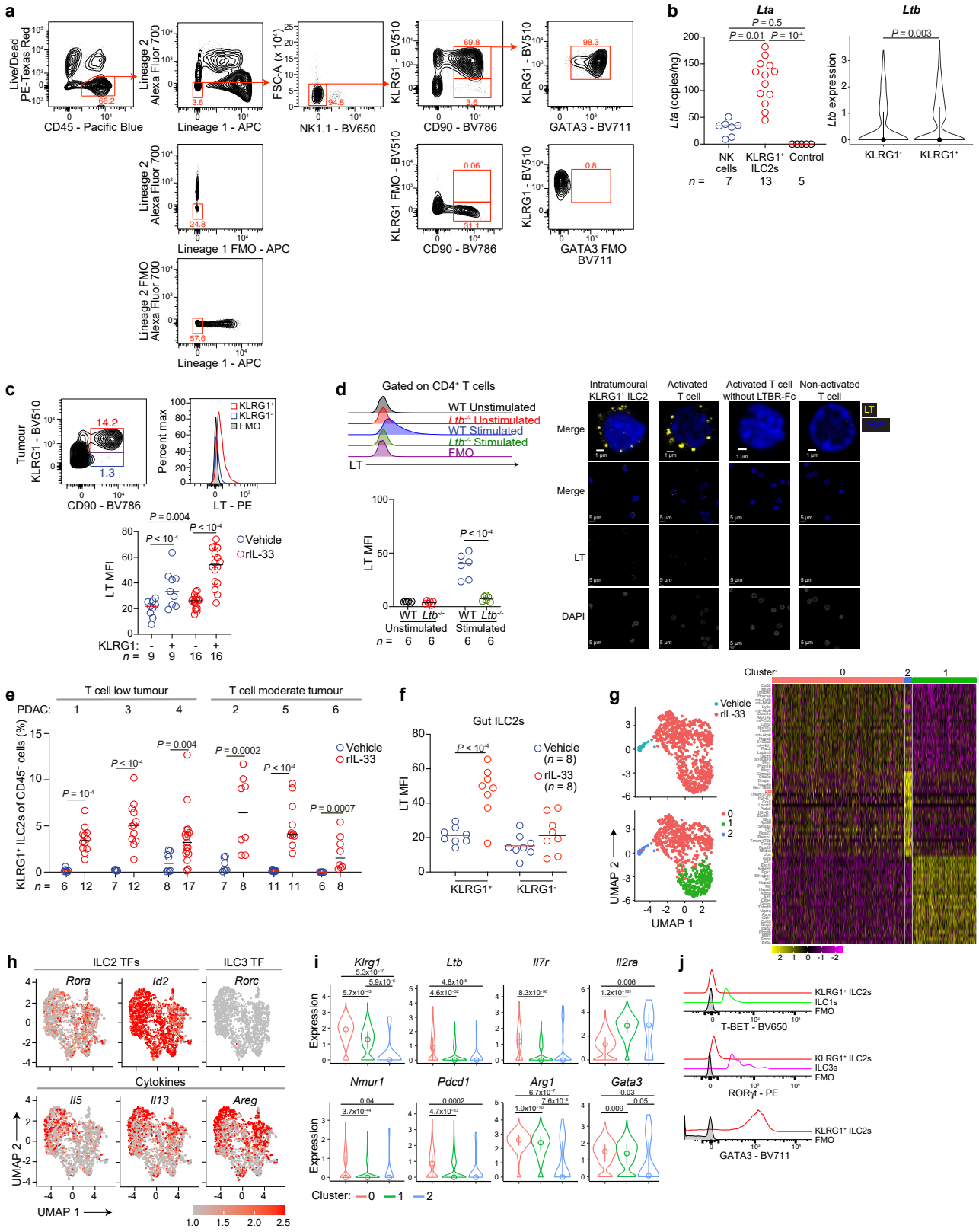

Extended Data Fig. 3 | See next page for caption.

Extended Data Fig. 3 | IL-33 expands LT-expressing KLRG1$^+$ ILC2s in PDAC mice. a, KLRG1$^+$ ILC2 gating strategy. **b**, *Lta* and *Ltb* mRNA expression in purified KLRG1$^+$ ILC2s (digital droplet PCR – **left**; scRNA-seq – **right**). **c, d, f**, LT expression on KLRG1$^+$ ILC2s by flow cytometry (**c**, rIL-33-treated PDAC mice; **f**, rIL-33-treated DSS-colitis mice), and confocal imaging of purified intratumoural KLRG1$^+$ ILC2s (**d**). In **d**, LT expression by flow cytometry (**left**) and confocal imaging (**right**) on αCD3 and αCD28-stimulated WT and *Ltb*$^{-/-}$ T cells (flow cytometry histograms) shown as positive and negative controls. **e**, Frequency of intratumoural KLRG1$^+$ ILC2s in rIL-33-treated PDAC mice. PDAC 1–6 = orthotopic PDAC mice established with PDAC cell lines 1–6. **g-i**, scRNA-seq of 794 purified tumour ILC2s (**g**) and 1,668 purified tumour and draining lymph node (DLN) ILC2s (**h, i**) from PDAC mice. Heat map = top 25 genes for each cluster. UMAP, violin plots = ILC transcription factors (**h**), and markers (**i**) in unsupervised clusters in Fig. 3a, and ILC2 cytokines (**h**). *Tbx21* was undetectable. **j**, ILC transcription factors on intratumoural KLRG1$^+$ ILC2s from rIL-33-treated PDAC mice by flow cytometry. Data collected 10 days (**g-j**) and 2 weeks (**b-f**) after tumour implantation, pooled from ≥2 independent experiments with $n \geq 2$ mice per group with consistent results. n = individual tumours from individual mice analysed separately. Horizontal bars = median; violin plots show the distribution with minima, maxima, and median (lines). P values by two-way ANOVA with Tukey's multiple comparisons test (**b left, e, f**), Wilcoxon signed rank test (**b, i** violin plots), two-way ANOVA with Holm's post-test (**c**), and two-way ANOVA with Sidak's multiple comparisons test (**d**).

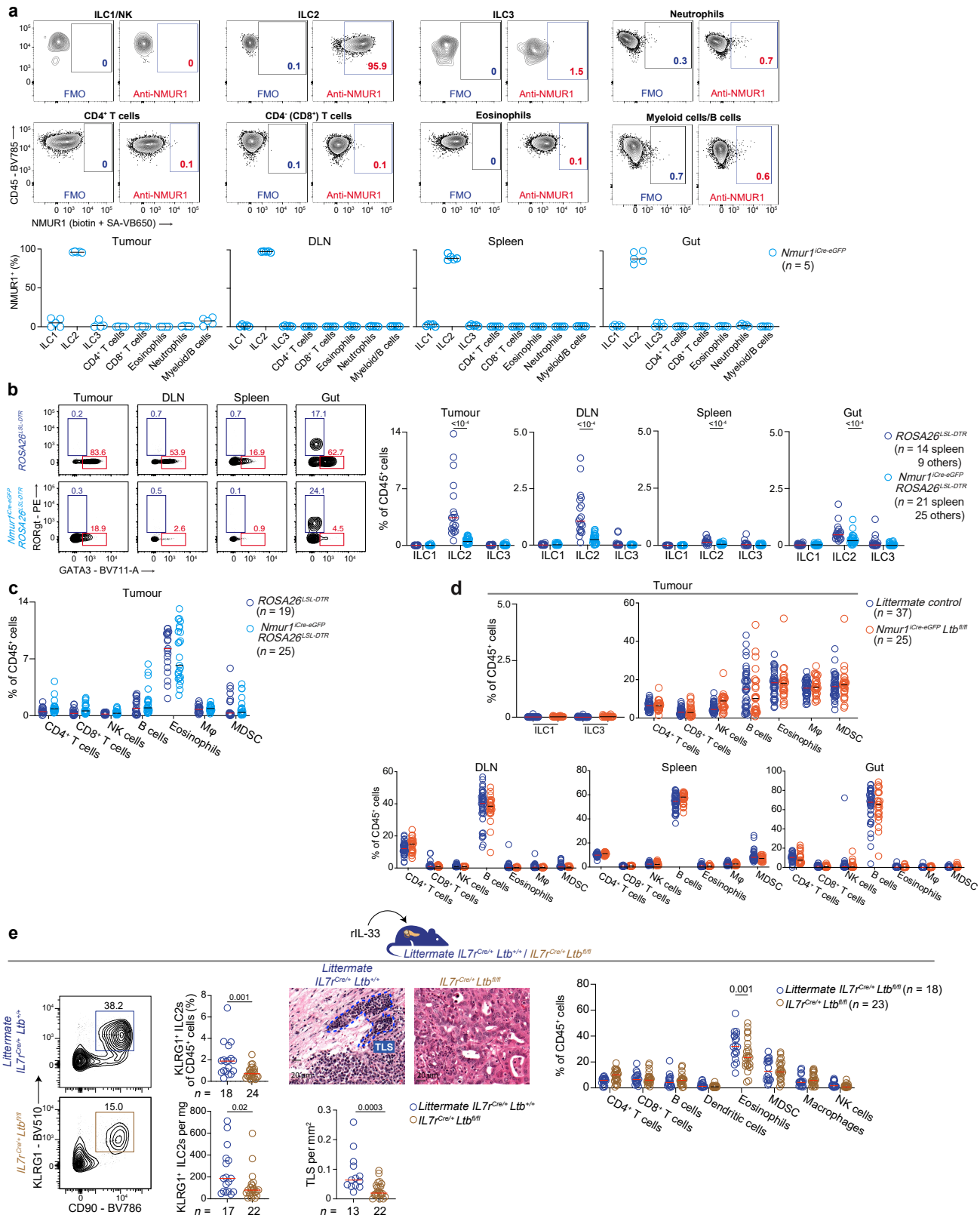

Extended Data Fig. 4 | Acute and conditional ILC2 deletion does not impact intratumoural ILC1s, ILC3s or non-ILC lymphocytes. a, NMUR1 expression on intratumoural immune cells in rIL-33-treated in *Nmur1*$^{iCre\text{-}eGFP}$ PDAC mice. **b, c**, Gating and frequency of all ILCs (**b**) and immune cells (**c**) in organs of rIL-33 and diphtheria toxin (DT)-treated *Nmur1*$^{iCre\text{-}eGFP}$*ROSA26*$^{LSL\text{-}DTR}$ and littermate control *ROSA26*$^{LSL\text{-}DTR}$ PDAC mice. **d**, Quantification of ILCs and immune cells in organs of rIL-33-treated *Nmur1*$^{iCre\text{-}eGFP}$ *Ltb*$^{fl/fl}$ and littermate control PDAC mice. **e**, Intratumoural KLRG1^{+} ILC2 gating, frequency and number (**left**), TLS density (**middle**) and immune cell frequency (**right**) in rIL-33-treated *Il7r*^{Cre}*Ltb*$^{fl/fl}$ and littermate control *Il7r*^{Cre}*Ltb*$^{+/+}$ PDAC mice. Dotted line = putative TLS. Data collected 2 (**b-e**) and 4 (**a**) weeks after tumour implantation, pooled from ≥2 independent experiments with $n \geq 3$ mice per group with consistent results. *n* = individual tumours or organs from individual mice analysed separately. Horizontal bars = median. In **d**, littermate control = *Ltb*$^{fl/+}$ and *Nmur1*$^{iCre\text{-}eGFP}$*Ltb*$^{fl/+}$ combined. *P* values by two-way ANOVA with Sidak's multiple comparison test (**b, e right**) and two-tailed Mann Whitney test (**e left, middle**).

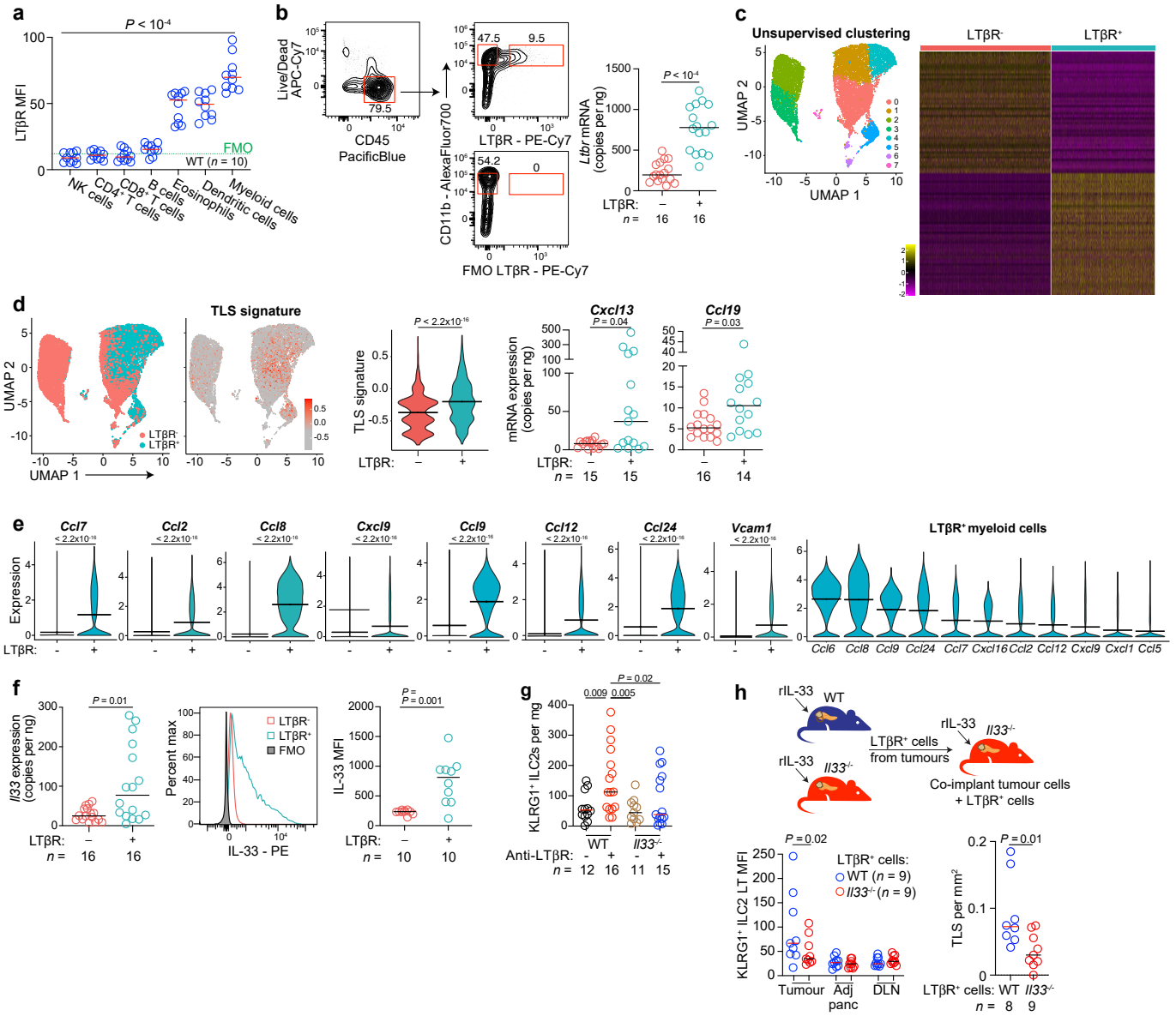

Extended Data Fig. 5 | Intratumoural LTβR$^+$ myeloid cells function as TLS organizers. a, LTβR expression in intratumoural immune cells in rIL-33-treated WT PDAC mice. **b**, Gating and *Ltbr* mRNA expression by digital droplet PCR in purified intratumoural LTβR$^+$ and LTβR$^-$ myeloid cells. **c**-**e**, scRNA-seq of 8,409 LTβR$^+$ and 6,220 LTβR$^-$ intratumoural myeloid cells purified from rIL-33-treated PDAC mice. In **c**, UMAP = cells by unsupervised clusters. Heat map = top 50 differentially expressed genes in LTβR$^+$ and LTβR$^-$ cells. **d**, Intratumoural LTβR$^+$ and LTβR$^-$ myeloid cell phenotypes by scRNA-seq (**left**) and TLS-inducing chemokine expression by digital droplet PCR (**right**). UMAP = cells by LTβR expression and TLS signature genes[7]. **e**, Violin plots of chemokines differentially (**left**) and globally (**right**) expressed by LTβR$^+$ cells. **f**, *Il33* mRNA expression (**left**) by digital droplet PCR and IL-33 protein (**right**) by flow cytometry in purified intratumoural myeloid cells. **g**, Intratumoural KLRG1$^+$ ILC2 density in agonist anti-LTβR-treated WT and *Il33*$^{-/-}$ PDAC mice. **h**, Experimental schema (**top**) and LT MFI of intratumoural KLRG1$^+$ ILC2s and intratumoural TLS density (**bottom**) in rIL-33-treated PDAC mice co-implanted with LTβR$^+$ cells purified from WT or *Il33*$^{-/-}$ PDAC mice. Data collected 4 (**a**) and 2 (**b**-**h**) weeks after tumour implantation, pooled from ≥2 independent experiments with $n \geq 2$ mice per group with consistent results. *n* = individual tumours from individual mice analysed separately. Horizontal bars = median; violin plots show the distribution with minima, maxima, and median (lines). MFI = mean fluorescence intensity. *P* values by one-way ANOVA test (**a**), two-tailed Mann-Whitney test (**b**, **d right**, **f**, **h**), Wilcoxon signed rank test (**d**, **e** violin plots), and two-way ANOVA with Sidak's multiple comparison test (**g**, **h** LT MFI).

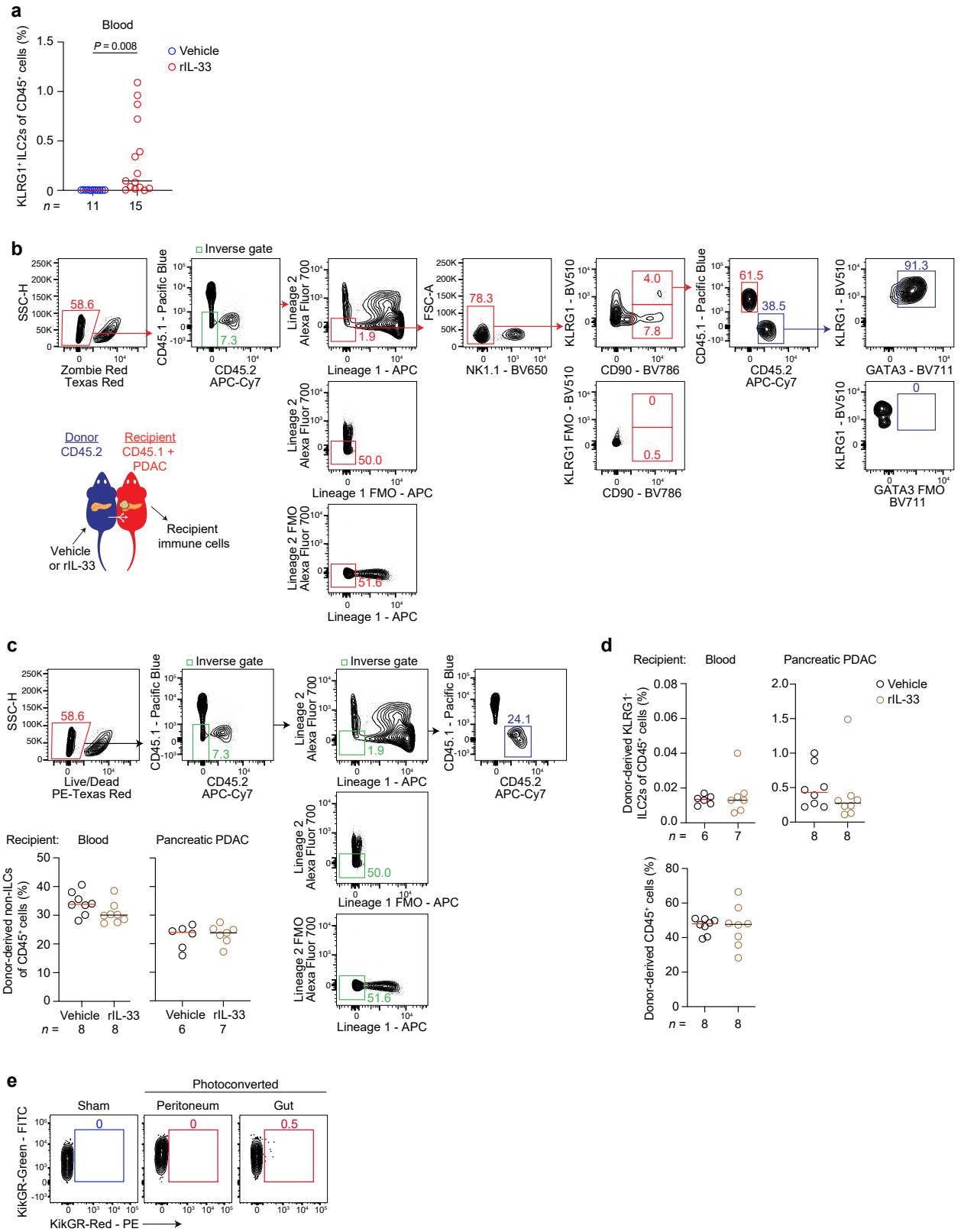

Extended Data Fig. 6 | ILC2 gating strategy and frequency in parabiotic PDAC mice. a, Frequency of KLRG1$^+$ ILC2s in blood of rIL-33-treated PDAC mice. **b-d**, Experimental schema and gating strategy (**b**) of donor and recipient KLRG1$^+$ ILC2s in recipient blood. Gating (**c**) and frequency of donor-derived non-ILCs (**c bottom**), KLRG1$^-$ ILC2s (**d top**) and CD45$^+$ cells (**d bottom**) in recipient blood and tumours. **e**, Gating in sham and photoconverted KikGR PDAC mice as in Fig. 4b; gated on KLRG1$^+$ ILC2s. Data collected 7 (**a-d**, blood) and 14 (**c, d**, tumour) days after tumour implantation, pooled from ≥2 independent experiments with $n \geq 3$ mice per group with consistent results. n = individual tumours or organs from individual mice analysed separately. Horizontal bars = median. P values by two-tailed Mann-Whitney test (**a, c, d**).

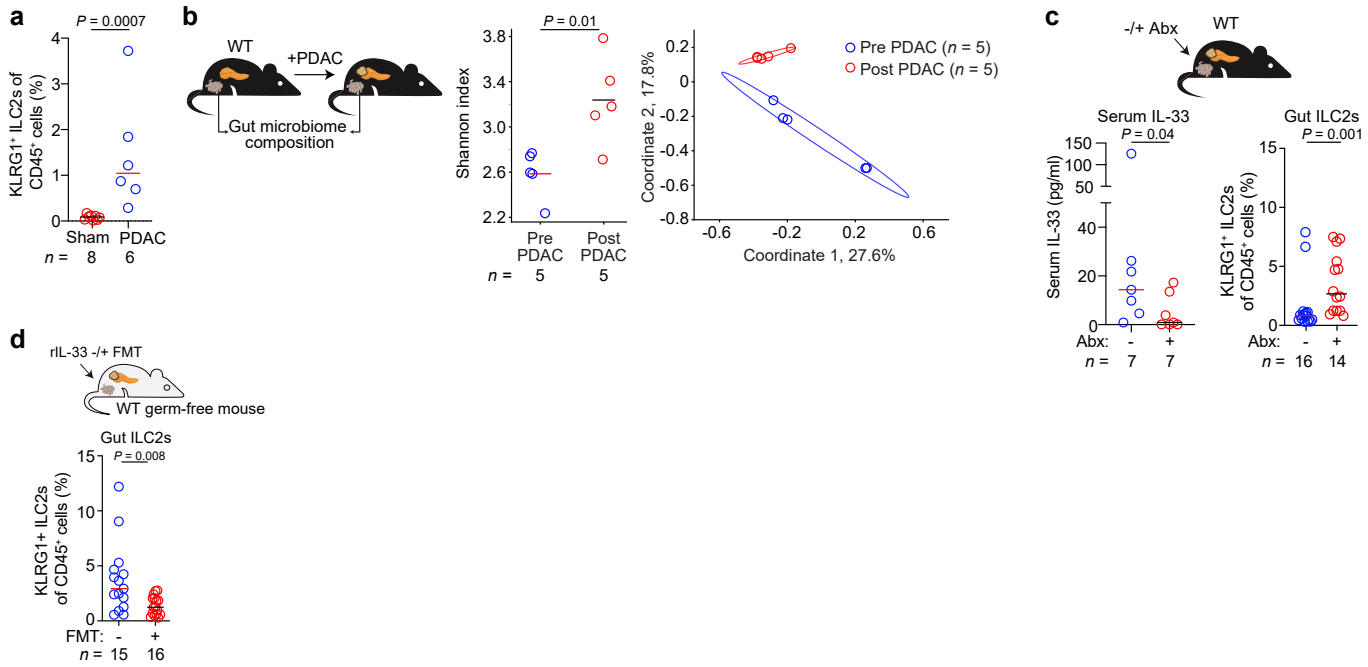

Extended Data Fig. 7 | PDACs alter diversity and composition of gut microbiota. a, Pancreatic KLRG1$^+$ ILC2 frequency in sham-treated and PDAC mice. **b**, Experimental schema and faecal microbiome analyses in PDAC mice by alpha diversity (Shannon index, **left**) and principal coordinate analysis (**right**). **c**, Experimental schema, serum IL-33, and gut KLRG1$^+$ ILC2s in rIL-33-treated PDAC mice with and without antibiotic (Abx) treatment. **d**, Gut KLRG1$^+$ ILC2s in germ-free PDAC mice with and without faecal microbial transplantation (FMT) from WT mice. Data collected 3 (**a, b**) and 4 (**c, d**) weeks after tumour implantation, pooled from ≥2 independent experiments with $n \geq 3$ mice per group with consistent results. *n* = individual measurements from individual mice analysed separately. Horizontal bars = median. *P* values by two-tailed Mann-Whitney test (**a, c, d**) and Welch's t-test (**b**).

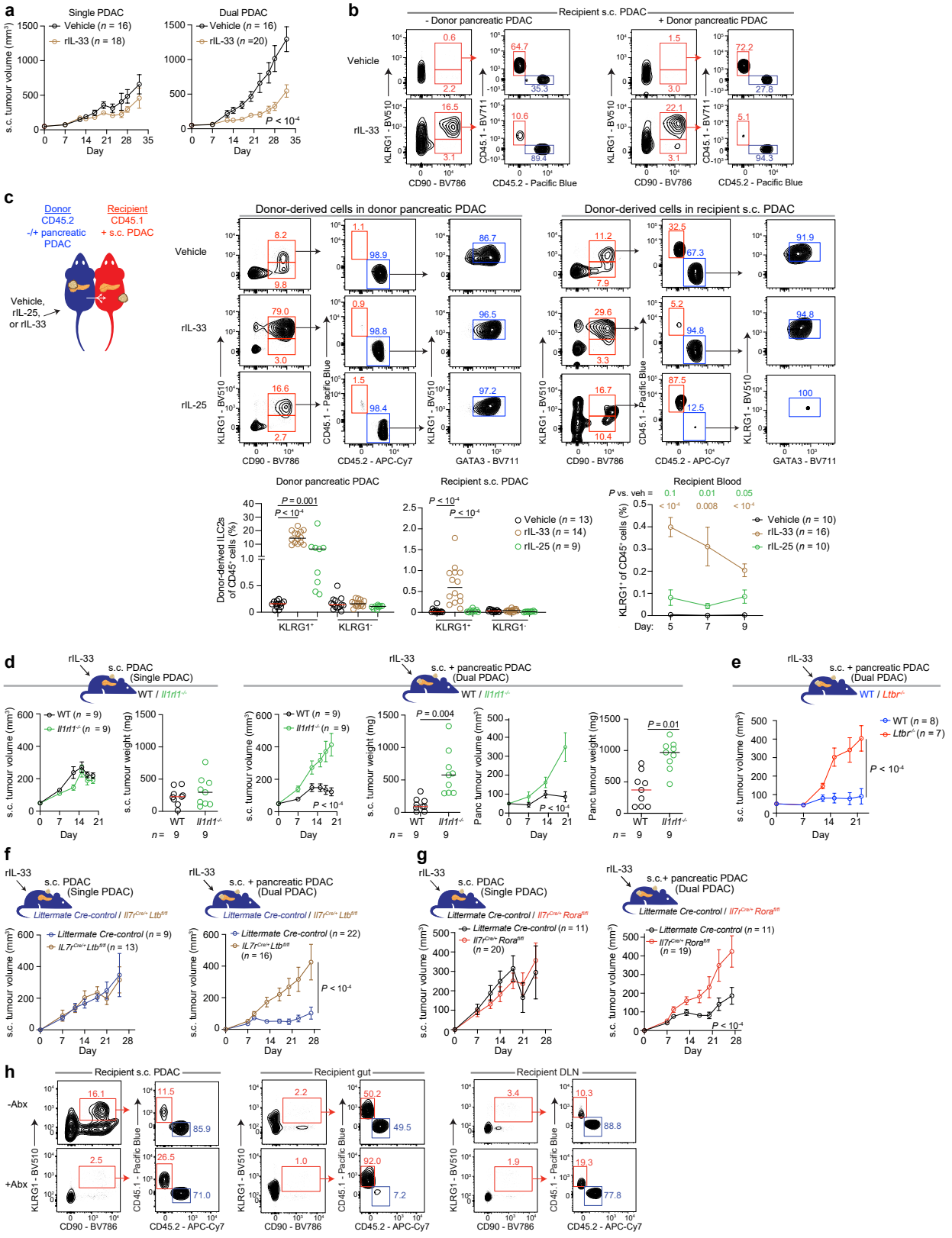

Extended Data Fig. 8 | See next page for caption.

Extended Data Fig. 8 | Molecular determinants of rIL-33-mediated dual PDAC control. a, Tumour volume in skin (subcutaneous (s.c.)) PDACs in vehicle-treated and rIL-33-treated mice with s.c. PDAC alone (single PDAC) or s.c. and pancreatic PDACs (dual PDAC). **b**, Gating of ILC2s from parabiotic mice with s.c. PDACs in recipients with/without pancreatic PDACs in donors as in Fig. 4f. **c**, Experimental schema (**left**), gating (**top**) and quantification of donor-derived ILC2s in donor pancreatic (**bottom left**), recipient s.c. PDAC (**bottom middle**) and blood (**bottom right**) in parabiotic PDAC mice treated with vehicle, rIL-33 or rIL-25. **d, e**, Tumour size in rIL-33-treated WT, *Il1rl1*$^{-/-}$ and *Ltbr*$^{-/-}$ s.c. PDAC (single) and s.c. + pancreatic (dual) PDAC mice. **f, g**, Tumour volume in s.c. PDACs in rIL-33-treated littermate Cre-control, *Il7r*$^{Cre/+}$*Ltb*$^{fl/fl}$ (**f**) and *Il7r*$^{Cre/+}$*Rora*$^{fl/fl}$ (**g**) single and dual PDAC mice. **h**, Gating of ILC2s from parabiotic mice with s.c. PDACs in recipients and pancreatic PDACs in donors treated with or without antibiotics (Abx) as in Fig. 4g. Data collected at 5–9 days (**c**, blood), 2 (**b, c**, tumour) and 3–5 (**d**) weeks post-implantation, pooled from ≥2 independent experiments with $n \geq 3$ mice per group with consistent results. *n* = individual tumours or organs from individual mice analysed separately. Horizontal bars = median. Cre-control littermates = *Il7r*$^{Cre/+}$*Ltb*$^{+/+}$ (**f**) and *Il7r*$^{Cre/+}$*Rora*$^{+/+}$ (**g**). *P* values by two-way ANOVA with Tukey's multiple comparison test (**a**), two-tailed Mann-Whitney test (**d** tumour weight) and two-way ANOVA with Sidak's multiple comparison test (all else).

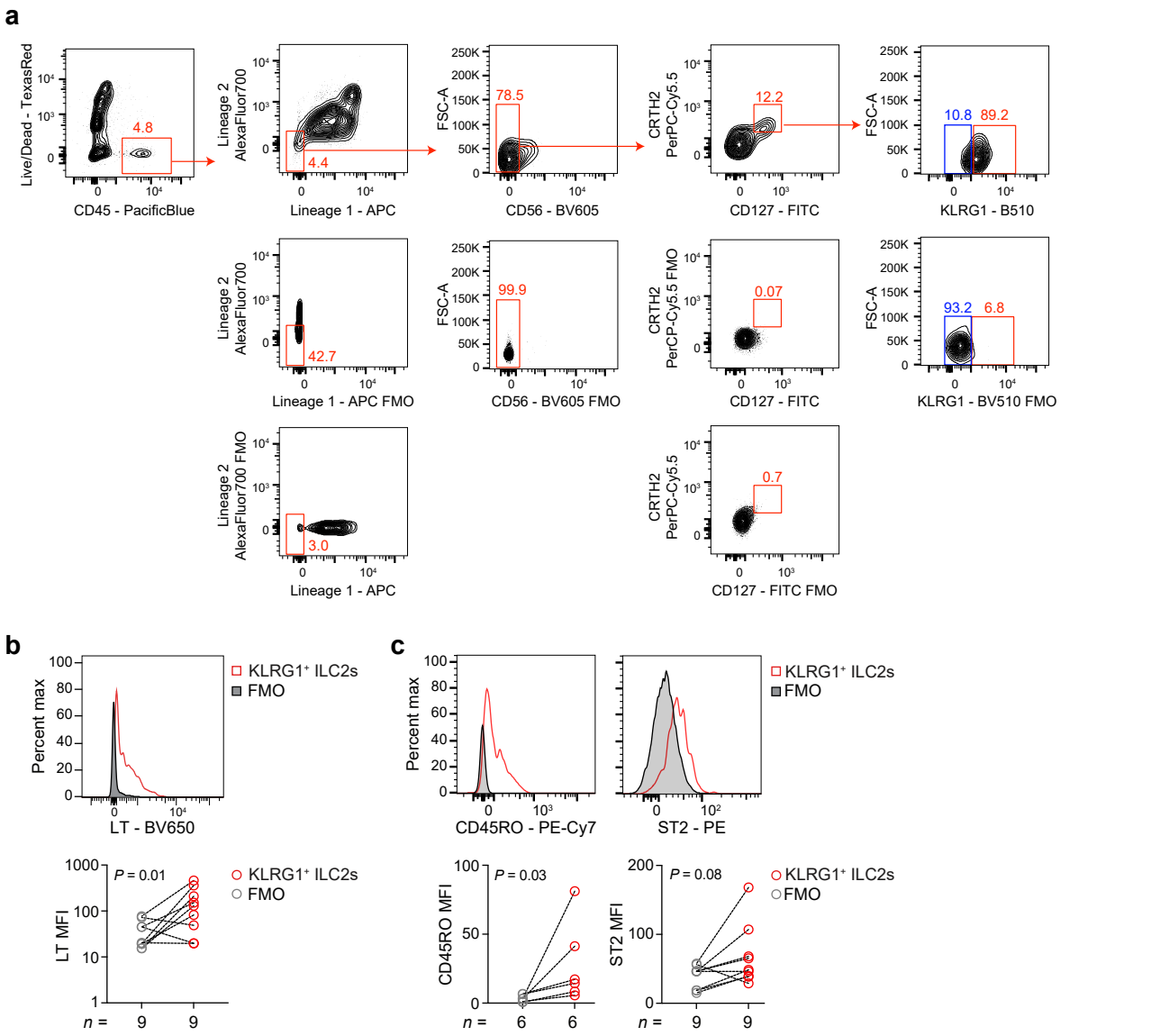

Extended Data Fig. 9 | Human intratumoural KLRG1⁺ ILC2 gating and phenotype. a-c, Gating strategy (**a**) and marker expression (**b, c**) on intratumoural KLRG1⁺ ILC2s in human PDACs. *n* = individual patients. MFI = mean fluorescence intensity. *P* values by paired two-tailed Mann Whitney test (**b, c**).

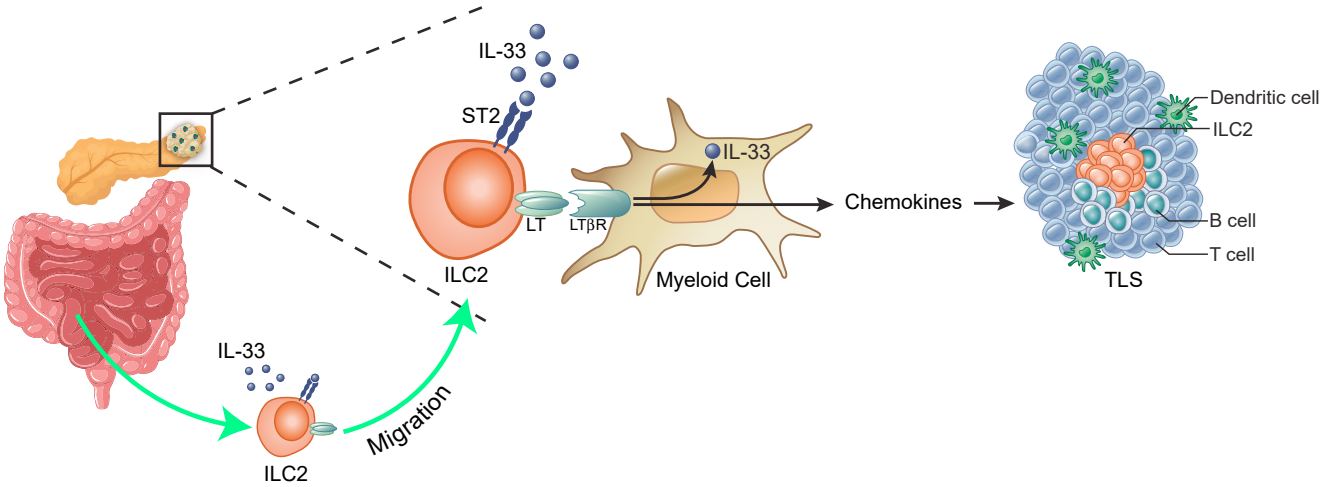

Extended Data Fig. 10 | The IL-33–ILC2–TLS pathway. Proposed schematic of IL-33–ILC2–TLS pathway. TLS: tertiary lymphoid structure.

nature research

Corresponding author(s): Vinod Balachandran

Last updated by author(s): 8/27/2024

Reporting Summary

Nature Research wishes to improve the reproducibility of the work that we publish. This form provides structure for consistency and transparency in reporting. For further information on Nature Research policies, see our Editorial Policies and the Editorial Policy Checklist.

Statistics

For all statistical analyses, confirm that the following items are present in the figure legend, table legend, main text, or Methods section.

n/a	Confirmed
☐	☒ The exact sample size (*n*) for each experimental group/condition, given as a discrete number and unit of measurement
☐	☒ A statement on whether measurements were taken from distinct samples or whether the same sample was measured repeatedly
☐	☒ The statistical test(s) used AND whether they are one- or two-sided *Only common tests should be described solely by name; describe more complex techniques in the Methods section.*
☐	☒ A description of all covariates tested
☐	☒ A description of any assumptions or corrections, such as tests of normality and adjustment for multiple comparisons
☐	☒ A full description of the statistical parameters including central tendency (e.g. means) or other basic estimates (e.g. regression coefficient) AND variation (e.g. standard deviation) or associated estimates of uncertainty (e.g. confidence intervals)
☐	☒ For null hypothesis testing, the test statistic (e.g. *F*, *t*, *r*) with confidence intervals, effect sizes, degrees of freedom and *P* value noted *Give P values as exact values whenever suitable.*
☒	☐ For Bayesian analysis, information on the choice of priors and Markov chain Monte Carlo settings
☒	☐ For hierarchical and complex designs, identification of the appropriate level for tests and full reporting of outcomes
☐	☒ Estimates of effect sizes (e.g. Cohen's *d*, Pearson's *r*), indicating how they were calculated

Our web collection on statistics for biologists contains articles on many of the points above.

Software and code

Policy information about availability of computer code

Data collection

For flow cytometry, all samples were analyzed on a FACS LSR Fortessa (BD Biosciences) using FlowJo (version 10.7.1, Tree Star).

Pathologic slides were digitized using Panoramic Flash 250 (3Dhistech, Budapest Hungary) using Zeiss 20x/0.8NA objective and custom filters for A488, A546, A594 and A647.

H&E: Slides were scanned on the Panoramic Scanner (3DHistech, Budapest, Hungary)

IHC: Nucleated cells in a TLS were determined and counted using the Analyze Particles function in ImageJ (ver. 2.3.0, NHI, USA). IL33+ cells in a TLS were counted manually.

IF: CD45 and IL33 positivity was determined by CaseViewer (3DHISTECH Ltd.).

Confocal: To visualize LT-PE and nuclear-DAPI, the images were taken on a point laser scanning confocal system (SP5, Leica, Wetzlar, Germany) with a 63x oil immersion objective 2.

Microbiome analysis: Pooled libraries were sequenced using Illumina MiSeq.

ST2 reporter assay: 630-nm wavelength absorbance detection was performed on a Cytation 3 reader (BioTek).

B cell receptor sequencing: Immunosequencing of the CDR3 regions of mouse B cell receptor chains was performed on genomic DNA from FFPE-fixed samples using the immunoSEQ Assay (Adaptive Biotechnologies)

ddPCR: Droplet generation was performed on a QX200 ddPCR system (Bio-Rad) using cDNA generated from 0.8-2 ng total RNA with the One-Step RT-ddPCR Advanced Kit for Probes (Bio-Rad) according to the manufacturer's protocol with reverse transcription at 42°C and annealing/

extension at 60°C. Each sample was evaluated in technical duplicates. Plates were read and analyzed (QuantaSoft) software to assess the number of droplets positive for genes of interest.

Data analysis

Statistical analyses were performed using R (version 4.0.3, single cell RNA sequencing) and Prism 9.2.0 (GraphPad Software, all else).

Tumor transcriptomic profiling: Data were analyzed using R (version 4.0.3).

Flow cytometry: Data were analyzed using FlowJo (version 10.7.1, Tree Star).

H&E: The number of TLSs were determined in at least 3 sections using QuPath ver.0.2.3.

IHC: Nucleated cells in a TLS were determined and counted using the Analyze Particles function in ImageJ ver. 2.3.0.

IF: IL33+ and IL33+CD45+ cells were quantified on ImageJ ver. 2.3.0, and cells per area estimated by calculating surface area based on presence of DAPI+ cells.

Confocal: The images with binomial signals were visualized using ImageJ ver. 2.3.0.

Single-cell RNA sequencing: Primary processing of sequencing images was done using Illumina's Real Time Analysis software (RTA). 10X Genomics Cell Ranger Single Cell Software suite v3.0.2 (https://support.10xgenomics.com/ single-cell-gene-expression/software/pipelines/ latest/what-is-cellranger) was used to demultiplex samples, align to mouse genomic reference mm10, filter, count UMIs, single-cell 5′ end genes, and control quality per the manufacturer's parameters. Processed data were subsequently analyzed in R (version 4.0.3).

Microbiome analysis: Demultiplexed raw reads were processed using Nextflow, nf-core ampliseq pipeline (version 2.4.0), with the following parameters: -profile singularity --FW_primer GTGYCAGCMGCCGCGGTAA --RV_primer CCGYCAATTYMTTTRAGTTT --dada_ref_taxonomy silva --ignore_empty_input_files --ignore_failed_trimming --min_frequency 10 --retain_untrimmed --trunclenf 240 --trunclenr 160. Specifically, reads were trimmed with cutadapt (https://doi.org/10.14806/ej.17.1.200), PhiX, and quality filtering, read pair merging, and amplicon sequence variant resolution was performed with DADA2. Subsequent taxonomic assignment was also performed with DADA2, using the Silva reference database, (version 138). Abundance tables were analyzed using the QIIME2 software package.

B cell receptor sequencing: Sequence data were processed and analyzed on the immunoSEQ Analyser web-based relational database.

Somatic hypermutation: Rearrangements with productive heavy chain sequences were retained for analysis of B cell clonal relationships, and clones were defined by VDJ-aware spectral clustering using the R package SCOPer. Mutation frequencies were computed using the observed mutations function in the R package Shazam

For manuscripts utilizing custom algorithms or software that are central to the research but not yet described in published literature, software must be made available to editors and reviewers. We strongly encourage code deposition in a community repository (e.g. GitHub). See the Nature Research guidelines for submitting code & software for further information.

Data

Policy information about availability of data

All manuscripts must include a data availability statement. This statement should provide the following information, where applicable:

- Accession codes, unique identifiers, or web links for publicly available datasets
- A list of figures that have associated raw data
- A description of any restrictions on data availability

Source data are provided for all experiments. RNA sequencing data from the TCGA and ICGC are publicly available. All other bulk RNA expression data are available under Gene Expression Omnibus (GEO) accession number GSE184585. scRNA-seq data of ILC2s have been previously reported and are available under GEO accession number GSE136720. scRNA-seq of myeloid cells are under GEO accession number GSE225990. 16s rRNA gene sequencing is available under BioProject ID number PRJNA944673.

All other data are available from the authors on reasonable request.

Field-specific reporting

Please select the one below that is the best fit for your research. If you are not sure, read the appropriate sections before making your selection.

☒ Life sciences ☐ Behavioural & social sciences ☐ Ecological, evolutionary & environmental sciences

For a reference copy of the document with all sections, see nature.com/documents/nr-reporting-summary-flat.pdf

Life sciences study design

All studies must disclose on these points even when the disclosure is negative.

Sample size

Sample sizes were determined based on our and other investigators experience with the respective cell lines used. No statistical methods were used as we observed many statistically significant effects in the data with the above methods of sample size selection without a priori sample size calculations.

Data exclusions

No data were excluded from the analyses.

Replication	All findings reported were reproducible and data shown are pooled from >=2 independent experiments, with comparable results in each experiment.
Randomization	6- to 14-week old mice were matched by age and sex and randomly assigned to specific treatment groups. Littermate controls were used as appropriate.
Blinding	No blinding was performed in experimental mouse interventions as knowledge of the treatment groups was required. All digital quantification was automated, with all experimental groups quantified in an identical fashion.

Reporting for specific materials, systems and methods

We require information from authors about some types of materials, experimental systems and methods used in many studies. Here, indicate whether each material, system or method listed is relevant to your study. If you are not sure if a list item applies to your research, read the appropriate section before selecting a response.

Materials & experimental systems

n/a	Involved in the study
☐	☒ Antibodies
☐	☒ Eukaryotic cell lines
☒	☐ Palaeontology and archaeology
☐	☒ Animals and other organisms
☐	☒ Human research participants
☒	☐ Clinical data
☒	☐ Dual use research of concern

Methods

n/a	Involved in the study
☒	☐ ChIP-seq
☐	☒ Flow cytometry
☒	☐ MRI-based neuroimaging

Antibodies

Antibodies used

Mouse Flow Antibody
Target Channel Antibody name Maker Catalog # Clone Amount (µ/50µL unless noted)
CD11b APC APC Rat Anti-Mouse CD11b BD Bioscience 553312 M1/70 0.5
CD11b APC-Cy7 APC-Cy7 Rat Anti-CD11b BD Bioscience 557657 M1/70 2
CD11c APC APC Hamster Anti-Mouse CD11c BD Bioscience 550261 HL3 0.5
CD11c BV510 Brilliant Violet 510 anti-mouse CD11c BioLegend 117338 N418 0.5
CD11c FITC Anti-Mo CD11c, FITC Invitrogen 11-0114-85 N418 0.5
CD127 FITC Anti-Mo CD127, FITC Invitrogen 11-1271-85 A7R34 1
CD127 PE-Cy7 PE/Cyanine7 anti-mouse CD127 BioLegend 135014 A7R34 1
CD19 PE PE anti-mouse CD19 BioLegend 115508 6D5 1
CD19 BV785 Brilliant Violet 875 anti-mouse CD19 BioLegend 115543 6D5 1
CD19 AF700 Anti-Mo CD19, Alexa Fuor 700 Invitrogen 65-0193-82 eBio1D3 1.25
CD25 PerCP-Cy5.5 PerCP-Cy5.5 anti-mouse CD25 BioLegend 102030 PC61 1.5
CD3 BV711 Brilliant Violet 711 anti-mouse CD3e BioLegend 100349 145-2C11 0.5
CD3 AF700 Anti-Mo CD3e, Alexa Fluor 700 Invitrogen 56-0032-82 17A2 1.25
CD4 BV711 BV711 anti-mouse CD4 BioLegend 100550 RM4-5 0.5
CD4 BV786 Brilliant Violet 76 anti-mouse CD4 BioLegend 100552 RM4-5 0.5
CD45 PacBlue Pacific Blue anti-mouse CD45 BioLegend 103126 30-F11 0.5
CD45.1 PacBlue Pacific Blue anti-mouse CD45.1 BioLegend 110722 A20 0.5
CD45.1 BV711 BV711 anti-mouse CD45.1 BioLegend 110739 A20 0.5
CD45.2 APC-Cy7 APC-Cy7 annti-mouse CD45.2 BioLegend 109824 104 0.5
CD5 APC APC Rat Anti-Mouse CD5 BD Bioscience 550035 53-7.3 0.5
CD8 BV510 Brilliant Violet (BV) 510 anti-mouse CD8a BioLegend 100751 53-6.7 2
CD90.2 BV786 BV786 Rat Anti-Mouse CD90.2 BD Bioscience 564365 53-2.1 0.5
DAPI PacBlue DAPI solution BD Bioscience 564907 1µl/1ml
DRAQ7 APC-Cy7 DRAQ7 BD Phermigen 51-9011172 1
F4/80 PE-Cy5 Anti-Mo F4/70, PE-Cy5 Invitrogen 15-4801-82 BM8 0.5
Fc-block n/a InVivoMab anti-mosue CD16/32 BioXCell BE0307 2.4G2 10µl/sample
FcER1 APC Anti-Mo FceRi alpha, APC Invitrogen 17-5898-82 "MAR-1" 0.5
GATA3 BV711 BV711 Mouse anti-GATA3 BD Horizon 565449 L50-823 2
GR-1 BV605 BV605 Rat Anti-Mouse Ly-6G and Ly-6C BD Bioscience 563299 RB6-8C5 0.3
IL-33 PE IL-33 Monoclonal antibody (396118) invitrogen MA5-23640 396118 10
IL17Rb PE PE anti-mouse IL17RB BioLegend 146306 9B10 1.25
Isotype of aIL-33 PE Rat IgG2a kappa Isotype Control, PE invitrogen 12-4321-80 eBR2a 1
KLRG1 BV510 Brilliant Violet 510 anti-mouse/human KLRG1 BioLegend 138421 2F1/KLRG1 1.25
LTBR PE-Cy7 PE/Cyanine7 anti-mouse lymphotoxin beta receptor antibody BioLegend 134410 5G11 0.5
MHC class2 AF700 Anti-Mo MHC Class II, Alexa Fluor 700 Invitrogen 56-5321-82 M5/114.15.2 0.5
NK1.1 BV650 BV650 anti-mouse NK1.1 BD Bioscience 564143 PK136 0.5
NK1.1 APC APC Mouse Anti-Mouse NK1.1 BD Phermigen 550627 PK136 0.5
NK1.1 BV605 Brilliant Violet 605 anti-mouse NK1.1 BioLegend 108740 PK136 0.5
NMUR1-biotinylated antibody clone 12-A03-A 0.0173 mg/ml

RORgt PE PE Mouse anti-Mouse RORgt BD Bioscience 562607 Q31-378 1.25
Secondary Ab of mLTBR-Fc PE R-phycoerythrin goat anti-mouse IgG2a conjugated Invitrogen P21139 0.5
Siglec-F APC APC anti-mouse CD170 (Siglec F) BioLegend 155508 S17007L 0.5
ST2 PE-Cy7 Anti-Mo IL-33R(ST2), PE-Cy7 Invitrogen 25-9335-82 RMST2-2 0.5
T-BET BV650 BV650 Mouse Anti-T-bet BD Bioscience 564142 O4-46 1.25
TCR Vb AF700 Anti-Mo TCR V beta 5.1/5.2, Alexa Fluor 700 Invitrogen 56-5796-82 MR-9-4 5
Zombie Red Tx-Red BioLegend 4231110 1µl/1ml
Streptavidin-BV650 Biolegend 405232 1:250

Human Flow Antibody
Target Channel Antibody name Maker Catalog # Clone Amount (µ/50µL)
GATA3 PE PE Mouse anti-GATA3 BD Biosciences 560074 L50-823 4
PD-1 BV786 BV786 Mouse Anti-Human CD279 (PD-1) BD Biosciences 563789 EH12.1 2
RORgt BV650 BV650 Mouse anti-Human RORgt BD Biosciences 563424 Q21-559 2
Secondary Ab for hLTBR-Fc BV650 BV650 Mouse Anti-Human IgG BD Biosciences 740596 G18-145 2
Secondary Ab for hLTBR-Fc PE PE Mouse Anti-Human IgG BD Biosciences 555787 G18-145 2
CD117 PE-Cy5 PE/Cy5 anti-human CD117 (c-kit) BioLegend 323412 A3C6E2 2
CD11b APC APC anti-human CD11b BioLegend 301310 ICRF44 2
CD161 BV785 Brilliant Violet 785 anti-human CD161 BioLegend 339930 HP-3G10 2
CD25 APC-Cy7 APC/Cy7 anti-human CD25 BioLegend 302614 BC96 2
CD45 PacBlue Pacific Blue anti-human CD45 BioLegend 304029 HI30 2
CD56 BV605 Brilliant Violet 605 anti-human CD56 (NCAM) BioLegend 318334 HCD56 2
CRTH2 PerCP-Cy5.5 PerCP/Cy5.5 anti-human CD294 (CRTH2) BioLegend 350116 BM16 4
CRTH2 PE PE anti-human CD294 (CRTH2) BioLegend 350106 BM16 4
FceRIa APC APC anti-Human FceRIa BioLegend 334612 AER-37 2
ICOS BV711 Brilliant Violet 711 anti-human/mouse/rat CD278 (ICOS) BioLegend 313548 C398.4A 2
NKp44 PE-Cy7 PE/Cy7 anti-human CD336 (NKp44) BioLegend 325116 P44-8 2
T-BET BV711 Brilliant Violet 711 anti-Tbet BioLegend 644820 4B10 2
TCR a/b AF700 Alexa Fluor 700 anti-human TCR a/b BioLegend 306730 IP26 2
KLRG1 BV510 Brilliant Violet 510 anti-mouse/human KLRG1 BioLegend 138421 2F1/KLRG1 2
CD11c APC Anti-Hu CD11c, APC Invitrogen 17-0116-42 3.9 2
CD127 FITC Anti-Hu CD127, FITC Invitrogen 11-1278-42 eBioRDR5 2
CD14 APC Anti-Hu CD14, APC Invitrogen 17-0149-42 61D3 2
CD16 APC Anti-Hu CD16 Invitrogen 17-0168-42 eBioCB16 2
CD19 AF700 Anti-Hu CD19 Invitrogen 56-0199-42 HIB19 2
CD3 AF700 Anti-Hu CD3, Alexa Fluor 700 Invitrogen 56-0037-42 OKT3 2
CD5 APC Ant-Hu CD5, APC Invitrogen 17-0058-42 L17F12 2
ST2 PE Anti-Hu IL-33R (ST2), PE Invitrogen 12-9338-42 hIL33Rcap 4

Recombinant Protein
Product name Maker Catalog # Application Concentration/Dose
rhLTBR/Fc Chimera R&D systems 629-LR Flow 2µg/ml, 30min
rmLTBR/Fc Chimera R&D systems 1008-LR Flow 1µg/ml, 30min, 4C
Recombinant Mouse IL-33 Protein R&D systems 3626-ML-010/CF Treatment (i.p.) 500 ng/body
Recombinant Mouse IL-25 Protein R&D systems 1399-ML-010/CF Treatment (i.p.) 500 ng/body
Diphtheria toxin (DT) EMD Millipore 322326 100 ng

in vivo/ vitro material
Product name Maker Catalog # Application Dose Details
Lymphotoxin beta Receptor Monoclonal Antibody Invitrogen 16-5671-82 Culture N/A Clone 3C8
Lymphotoxin beta Receptor Monoclonal Antibody Invitrogen 16-5671-38 Vivo 100µg/ injection Clone 3C8
Rat IgG1 kappa Isotype control Invitrogen 16-4301-38 vivo 100µg/ injection Isotype for aLTBR agonist

Validation

All antibodies were validated by the manufacturer and used per their instructions. In our experiments, isotype and/or FMO control samples were included. Additional information on validation can be found on the manufacturers' websites.

Eukaryotic cell lines

Policy information about cell lines

Cell line source(s)

All tumor cell lines were derived from KPC (Pdx1-Cre;LSL-KrasG12D/+;LSL-Trp53R172H/+) or KPCY (Pdx1-Cre;LSL-KrasG12D/+;LSL-Trp53R172H/+; Rosa26YFP/YFP) mice and were gifts from R.H. Vonderheide and B.J Stanger. The HEK-Blue-IL33 cell line was obtained from Invivogen.

Authentication

All cell lines were authenticated as bonafide pancreatic cancer cell lines. This was based on histopathologic verification by a dedicated pancreatic cancer pathologist that these cell lines generate tumors on intra-pancreatic implantation that faithfully recapitulate features of both human pancreatic cancers and pancreatic cancers that develop in spontaneous genetically engineered mice.

Mycoplasma contamination

Cell lines were regularly tested using MycoAlert Mycoplasma Detection Kit (Lonza). None of the cell lines used in this study tested positive for Mycoplasma.

Commonly misidentified lines
(See ICLAC register)

No commonly misidentified lines were used in this study.

Animals and other organisms

Policy information about studies involving animals; ARRIVE guidelines recommended for reporting animal research

Laboratory animals	C57BL/6 (wild-type [WT], CD45.2) and C57BL/6 CD45.1 mice were purchased from Jackson Laboratory. Il1rl1−/− (ST2 deficient) and Il33-/- mice were a gift from M.J. Rosen. Ltbfl/fl mice were a gift from A.V. Tumanov. Nmur1iCre-eGFP ROSALSL-DTR mice are previously described24. Ltbfl/fl was crossed to Nmur1iCre-eGFP and Il7rCre/+ to obtain Nmur1iCre-iGFP Ltbfl/fl and Il7rCre/+Ltbfl/fl mice. Il7rCre/+Rorafl/fl mice were a gift from A.N.J. McKenzie. Ltbr-/- mice were a gift from T.T. Lu. CAG-KikGR33 mice were a gift from G.E. Diehl. Germ-free mice were provided by the gnotobiotic facility at Weill Cornell Medical Center (MSK). For all experiments, 6-14-week old mice were age, and sex-matched and randomly assigned to specified treatment groups, with at least two independent experiments performed throughout. Both male and female animals were utilized. Animals were bred and maintained in a specific pathogen-free animal facility at Memorial Sloan Kettering Cancer Center.
Wild animals	No wild animals were used.
Field-collected samples	No field-collected samples were used in this study.
Ethics oversight	Animals were bred and maintained in a specific pathogen-free animal facility, and all experiments were conducted in accordance with an Institutional Animal Care and Use Committee (IACUC) approved protocol at Memorial Sloan Kettering Cancer Center (MSK) and in compliance with all relevant ethical regulations.

Note that full information on the approval of the study protocol must also be provided in the manuscript.

Human research participants

Policy information about studies involving human research participants

Population characteristics	Clinical characteristics of patients in the tissue microarray, flow cytometry, ILC2 culturing, and transcriptomic cohorts are outlined in Supplementary Tables 1, 2, 3, and 5 and are provided below. Clinicopathological characteristics of PDAC patients in MSK transcriptome cohort (n = 82) Characteristic n (%) Sex Male 40 (49) Female 42 (51) Age (y) Median (IQR) 68 (62-75) Tumor location Head 53 (65) Body/tail 29 (35) Procedure Pancreaticoduodenectomy 53 (65) Distal pancreatectomy 29 (35) pT 1 2 (2) 2 1 (1) 3 78 (95) 4 1 (1) pN 0 33 (40) 1 48 (59) x 1 (1) pM 0 81 (99) 1 1 (1) Pathological Stage IA 2 (2) IB 1 (1) IIA 30 (37) IIB 47 (57) III 1 (1) IV 1 (1) Surgical margin Positive 9 (11) Negative 71 (87) NA 2 (2) Adjuvant Treatment Yes 61 (74) No 21 (26) Clinicopathological characteristics of PDAC patients in IHC and IF cohort (n = 11) Characteristic n (%) Sex

Male 4 (36)
Female 7 (64)
Age (y)
Median (IQR) 70 (62-79)
Tumor location
Head 9 (82)
Body/tail 2 (18)
Procedure
Pancreaticoduodenectomy 9 (82)
Distal pancreatectomy 2 (18)
pT
1 0 (0)
2 0 (0)
3 11 (100)
4 0 (0)
pN
0 5 (45)
1 6 (55)
pM
0 11 (100)
1 0 (0)
Pathological stage
IIA 5 (45)
IIB 6 (55)
Surgical margin
Positive 4 (36)
Negative 7 (64)
Adjuvant treatment
Yes 11 (100)
No 0 (0)

Clinicopathological characteristics of PDAC patients in flow cytometry cohort (n = 9)
Characteristic n (%)
Sex
Male 4 (44)
Female 5 (55)
Age (y)
Median (IQR) 67 (63-80)
Procedure
Pancreaticoduodenectomy 6 (66)
Distal pancreatectomy 2 (22)
Total pancreatectomy 1 (11)
pT
1 4 (44)
2 3 (33)
3 1 (11)
4 0 (0)
x 1 (11)
pN
0 4 (44)
1 1 (11)
2 2 (22)
x 2 (22)
pM
0 4 (54)
1 1 (11)
2 3 (33)
x 1 (11)
Pathological stage
I 3 (33)
II 2 (22)
III 3 (33)
Local recurrence 1 (11)
Surgical margin
Positive 0 (0)
Negative 9 (100)
Adjuvant treatment
Yes 7 (77)
No 2 (22)

Clinicopathological characteristics of PDAC patients with serum IL33 measurements (n = 77)

Characteristic n (%)
Sex
Male 43 (56)
Female 34 (44)

Pathological stage
I 32 (42)
II 43 (56)
III 2 (2)
Neoadjuvant treatment
Yes 26 (34)
No 51 (66)
Adjuvant treatment
Yes 66 (86)
No 8 (10)
Unknown 3 (4)

Recruitment

All patients eligible for surgical resection at Memorial Sloan Kettering Cancer Center were recruited to participate in an Institutional Review Board-approved protocol. All patients who provided informed consent had samples collected; all study procedures were conducted in strict compliance with all ethical and institutional regulations. As patients were only recruited at Memorial Sloan Kettering Cancer Center, there is the potential for institution-specific selection bias. We do not believe that this potential bias would impact the results of this study.

All tumor samples were surgically resected primary PDACs (for tumor transcriptomic profiling or serum IL33 measurement) or surgically resected human PDAC (flow cytometry,). The human PDAC tissue microarrays, PDAC RNA sequencing from the ICGC, and human tumor sequencing from the TCGA have been previously described.

Ethics oversight

All tissues were collected at Memorial Sloan Kettering Cancer Center under study protocol #15-149 that was approved by the Memorial Sloan Kettering Cancer Center Institutional Review Board. Informed consent was obtained for all patients. The study was in strict compliance with all institutional ethical regulations.

Note that full information on the approval of the study protocol must also be provided in the manuscript.

Flow Cytometry

Plots

Confirm that:

☒ The axis labels state the marker and fluorochrome used (e.g. CD4-FITC).

☒ The axis scales are clearly visible. Include numbers along axes only for bottom left plot of group (a 'group' is an analysis of identical markers).

☒ All plots are contour plots with outliers or pseudocolor plots.

☒ A numerical value for number of cells or percentage (with statistics) is provided.

Methodology

Sample preparation

Mouse and human PDACs and mouse intestines were mechanically dissociated and incubated in collagenase (collagenase II for murine tumors, collagenase IV for human tumors, both 5 mg/ml; Worthington Biochemical Corp., Fisher Scientific), DNAse I (0.5 mg/ml; Roche Diagnostics), and Hank's balanced salt solution (Gibco, Fisher Scientific) for 30 minutes at 37°C. Digestion was then quenched with fetal bovine serum (FBS, Life Technologies). Digested tumors and DLNs were then mechanically disassociated and filtered through 100- and 40-mm nylon cell strainers (Falcon, Fisher Scientific) using PBS with 5% FBS (Life Technologies) and 2 mM EDTA (pH8.0, Invitrogen). Spleens were mechanically dissociated and filtered through 70- and 40-mm nylon cell strainers (Falcon, Fisher Scientific) using PBS with 5% FBS and 2 mM EDTA, followed by RBC lysis (RBC lysis buffer, Invitrogen Scientific). Peripheral blood was processed with RBC lysis and filtered through 40-mm nylon cell strainers. Mouse Fc receptors were blocked with FceRIII/II-specific antibody (1 mg per 1 x 106 cells; clone 2.4G2, Bio XCell).

Instrument

Flow cytometry data were collected on a BD LSR Fortessa (BD Biosciences). Flow cytometry sorting was performed on a BD FACS Aria (BD Biosciences).

Software

Data were analyzed using FlowJo Software (version 10.7.1, Tree Star).

Cell population abundance

For ILC2 transfer, live, CD45+, lineage−, CD90+, KLRG1+ ILC2s from tumors were sort-purified to 98% purity at day 10 post-implantation using an Aria Cell Sorter (BD Biosciences)

For myeloid cell transfer, live, CD45+, NK1.1-, CD11b+, LTBR+ cells were sort-purified to 90% purity using an Aria Cell Sorter.

Gating strategy

Mouse ILC2s were defined as live, CD45+, lineage− (CD3, CD5, NK1.1, CD11b, CD11c, CD19, FceR1), CD90+. All live, CD45+, lineage−, CD90+ cells were GATA3+ (Extended Data Figure 3a).

Mouse KLRG1+ were defined as live, CD45+, lineage− (CD3, CD5, NK1.1, CD11b, CD11c, CD19, FceR1), CD90+, KLRG1+.

The following definitions were used for other immune cells:
ILC1 - live, CD45+, lineage-, Tbet+
ILC3 - live, CD45+, lineage-,NK1.1-, Rorgt+
NK - live, CD45+, CD3-, NK1.1+
B cell - live, CD45+, CD3-, NK1.1-, CD19+
CD4+ T cell - live, CD45+, NK1.1-, CD3+, CD8-, CD4+

CD8+ T cell - live, CD45+, NK1.1-, CD3+, CD4-, CD8+
Eosinophils - live, CD45+, NK1.1-, CD3-, CD19-, CD11b+ SiglecF+
Macrophage - live, CD45+, NK1.1-, CD3-, CD19-, CD11b+ , F4/80+
Myeloid derived suppressor cell (MDSC) - live, CD45+, NK1.1-, CD3-, CD19-, CD11b+ SiglecF- Gr-1+
Dendritic cells (DCs) - live, CD45+, NK1.1-, CD3-, CD19-, Gr-1-, F4/80-, CD11c+, MHC-II+

Human ILC2s were defined as live, CD45+, lineage– (CD3, CD5, CD56, CD11b, CD11c, CD14, CD16, CD19, TCRa/b, FceR1), CD127+, CRTH2+.

Human KLRG1+ ILC2s were defined as live, CD45+, lineage– (CD3, CD5, CD56, CD11b, CD11c, CD14, CD16, CD19, TCRa/b, FceR1), CD127+, CRTH2+, KLRG1+.

☒ Tick this box to confirm that a figure exemplifying the gating strategy is provided in the Supplementary Information.